Monthly Notices
of the
ROYAL ASTRONOMICAL SOCIETY

MNRAS **458,** 1559–1580 (2016)
Advance Access publication 2016 February 17

doi:10.1093/mnras/stw374

Baryonic impact on the dark matter distribution in Milky Way-sized galaxies and their satellites

Qirong Zhu,[1,2]★ Federico Marinacci,[3]★ Moupiya Maji,[1,2] Yuexing Li,[1,2] Volker Springel[4,5] and Lars Hernquist[6]

[1]*Department of Astronomy & Astrophysics, The Pennsylvania State University, 525 Davey Lab, University Park, PA 16802, USA*
[2]*Institute for Gravitation and the Cosmos, The Pennsylvania State University, University Park, PA 16802, USA*
[3]*Department of Physics, Kavli Institute for Astrophysics and Space Research, Massachusetts Institute of Technology, Cambridge, MA 02139, USA*
[4]*Heidelberg Institute for Theoretical Studies, Schloss-Wolfsbrunnenweg 35, D-69118 Heidelberg, Germany*
[5]*Zentrum für Astronomie der Universität Heidelberg, ARI, Mönchhofstr. 12-14, D-69120 Heidelberg, Germany*
[6]*Harvard-Smithsonian Center for Astrophysics, Harvard University, 60 Garden Street, Cambridge, MA 02138, USA*

Accepted 2016 February 12. Received 2016 February 12; in original form 2015 June 12

ABSTRACT

We study the impact of baryons on the distribution of dark matter in a Milky Way-sized halo by comparing a high-resolution, moving mesh cosmological simulation with its dark matter-only counterpart. We identify three main processes related to baryons – adiabatic contraction, tidal disruption, and reionization – which jointly shape the dark matter distribution in both the main halo and its subhaloes. The relative effect of each baryonic process depends strongly on the subhalo mass. For massive subhaloes with maximum circular velocity $v_{\rm max} > 35\,{\rm km\,s^{-1}}$, adiabatic contraction increases the dark matter concentration, making these haloes less susceptible to tidal disruption. For low-mass subhaloes with $v_{\rm max} < 20\,{\rm km\,s^{-1}}$, reionization effectively reduces their mass on average by ≈30 per cent and $v_{\rm max}$ by ≈20 per cent. For intermediate subhaloes with $20\,{\rm km\,s^{-1}} < v_{\rm max} < 35\,{\rm km\,s^{-1}}$, which share a similar mass range as the classical dwarf spheroidals, strong tidal truncation induced by the main galaxy reduces their $v_{\rm max}$. As a combined result of reionization and increased tidal disruption, the total number of low-mass subhaloes in the hydrodynamic simulation is nearly halved compared to that of the *N*-body simulation. We do not find dark matter cores in dwarf galaxies, unlike previous studies that employed bursty feedback-driven outflows. The substantial impact of baryons on the abundance and internal structure of subhaloes suggests that galaxy formation and evolution models based on *N*-body simulations should include these physical processes as major components.

Key words: methods: numerical – galaxies: evolution – dark matter.

1 INTRODUCTION

A major achievement in observational cosmology is the discovery that our Universe is composed of ∼4 per cent baryons, 20 per cent dark matter (DM), and 76 per cent dark energy (DE; Frieman, Turner & Huterer 2008). The first observational evidence for DM dates back to 1933 when Zwicky noted a missing mass problem in the Coma cluster of galaxies: the visible galaxies account for only a small fraction of the total mass inferred from the dynamics (Zwicky 1937). More evidence came later from galactic rotation curves in spiral galaxies (Rubin, Ford & Thonnard 1980), gravitational lensing, and the Bullet cluster which shows an offset of the centre of the total mass from that of the baryons (Clowe et al. 2006). The first compelling observational evidence for DE was found later in 1998 when two teams studying Type Ia supernovae (SNe) independently found that the expansion of the Universe is accelerating (Riess et al. 1998; Perlmutter et al. 1999). This finding has been confirmed by subsequent SN observations, and independent evidence from galaxy clusters (e.g. Vikhlinin et al. 2006; Allen, Evrard & Mantz 2011), large-scale structure (e.g. Tegmark et al. 2006; Addison, Hinshaw & Halpern 2013), and the cosmic microwave background (e.g. Spergel et al. 2007; Komatsu et al. 2011; Hinshaw et al. 2013; Planck Collaboration XIII 2015).

These observations motivate the current 'standard model' of cosmology (ΛCDM), where dark energy and cold dark matter shape the formation and evolution of cosmic structures (e.g. Frenk & White 2012; Kravtsov & Borgani 2012; Conselice 2014; Somerville & Davé 2015). To date, numerous ΛCDM cosmological simulations have produced clumpy and filamentary large-scale structures as seen

★ E-mail: zhuqirong1874@gmail.com (QZ); fmarinac@mit.edu (FM)

in galaxy surveys (e.g. Navarro, Frenk & White 1997; Springel et al. 2005b; Springel, Frenk & White 2006; Gao et al. 2012; Vogelsberger et al. 2014c), and have confirmed that structures form through hierarchical assembly in CDM-dominated universes. However, on small scales (i.e. less than ∼10 kpc), there appear to be a number of tensions between predictions from the ΛCDM model and observations, notably (1) the 'missing satellites problem', in which the abundance of subhaloes produced by *N*-body simulations is orders of magnitude larger than the two dozens of satellites observed in the Milky Way (MW; e.g. Klypin et al. 1999; Moore et al. 1999; Kravtsov, Gnedin & Klypin 2004; Kravtsov 2010); (2) the 'too big to fail problem', in which *N*-body simulations produce overly dense massive subhaloes compared to the brightest dwarf galaxies in the MW and Local Group (Boylan-Kolchin, Bullock & Kaplinghat 2011, 2012; Garrison-Kimmel et al. 2014b; Tollerud, Boylan-Kolchin & Bullock 2014); and (3) the 'core-versus-cusp problem', in which the central dark matter density profiles of DM-dominated dwarf spheroids (dSphs) are observed to apparently feature smooth cores instead of the cusps that are generically predicted by CDM models (e.g. Gilmore et al. 2007; Evans, An & Walker 2009; de Blok 2010; Strigari, Frenk & White 2010; Amorisco & Evans 2012; Martinez 2015). These problems have motivated alternative models such as self-interacting DM (Davé et al. 2001; Vogelsberger, Zavala & Loeb 2012; Elbert et al. 2015; Vogelsberger et al. 2014a) or warm DM (e.g. Kennedy et al. 2014; Polisensky & Ricotti 2014; Schneider et al. 2014).

However, some of the discrepancies were reported in DM-only simulations in which the dynamical coupling between baryons and DM was ignored. While this assumption may be justified on large scales, this is no longer the case on kpc scales, where the density starts to be dominated by baryons, and the dynamics becomes governed by baryonic processes such as gas dynamics, star formation, black hole accretion, and feedback from stars and active galactic nuclei (AGN).

An impact of baryons on the DM arises from different spatial distributions of the two components. A well-known effect is adiabatic contraction (Young 1980; Barnes & White 1984; Blumenthal et al. 1986; Ryden & Gunn 1987; Gnedin et al. 2004, 2011; Zemp et al. 2012; Pillepich et al. 2014), which causes an increase of the mass concentration of DM in the centre of a galaxy due to gas inflow as a result of cooling. The increased DM mass concentration and the presence of a stellar disc can produce stronger tidal forces, which have been suggested as a way to significantly affect the abundance and distribution of subhaloes and satellite galaxies in the MW (e.g. D'Onghia et al. 2010a; Peñarrubia et al. 2010; Zolotov et al. 2012; Arraki et al. 2014).

Hydrodynamic simulations have become powerful tools to investigate the response of DM to baryons and vice versa, thanks to recent progress in numerical methods (e.g. Springel 2010; Read & Hayfield 2012; Hopkins 2013; Hu et al. 2014) and physical modelling (Aumer et al. 2013; Stinson et al. 2013; Vogelsberger et al. 2013; Hopkins et al. 2014) that improved upon long-standing issues in the field (Agertz et al. 2007; Sijacki et al. 2012; Torrey et al. 2012). Recent cosmological simulations such as the Illustris (Vogelsberger et al. 2014c) and EAGLE (Schaye et al. 2015) projects were able to reproduce different galaxy populations that resemble the observed ones both locally and in the high-redshift Universe (e.g. Genel et al. 2014; Vogelsberger et al. 2014b). In particular, Vogelsberger et al. (2014c) showed that subhaloes in DM-only simulation are more prone to tidal disruption than those in hydrodynamic simulations, leading to a depletion of satellites near galaxy cluster centres and a drop in the matter power spectrum on small scales.

Several solutions have been proposed to solve the 'too big to fail' problem, including tidal effects (Zolotov et al. 2012; Arraki et al. 2014), which however might be insufficient in some cases (for instance in M31; see Tollerud et al. 2014), a mass-dependent abundance of subhaloes which may alleviate the problem if a lower total mass of the MW is assumed (Wang et al. 2012; Vera-Ciro et al. 2013; Sawala et al. 2014), and strong outflows driven by SN explosions which can have a direct impact on the central DM content in dwarf galaxies, possibly leading to a cored profile (e.g. Navarro, Frenk & White 1996; Governato et al. 2012; Teyssier et al. 2013; Brooks & Zolotov 2014; Madau, Shen & Governato 2014; Ogiya & Burkert 2015). However, Boylan-Kolchin et al. (2012) and Garrison-Kimmel et al. (2013) argue that the required energy from SNe may not be sufficient given the low stellar mass in some of the dwarf galaxies (but see also the energy argument by Madau et al. 2014). Moreover, most hydrodynamic simulations (e.g. Mashchenko, Wadsley & Couchman 2008; Governato et al. 2012; Teyssier et al. 2013; Madau, Shen & Governato 2014) are focused on dwarf galaxies in field environments, which may not be representative for the dwarfs in the MW or M31.

In order to investigate baryonic effects on DM in dwarf galaxies of the MW, we need high-resolution, cosmological hydrodynamic simulations which produce a spiral galaxy with properties similar to those of the MW. Producing MW-like disc galaxies in cosmological simulations has been a decade-long challenge, but recently several groups have succeeded in this endeavour (Agertz, Teyssier & Moore 2011; Guedes et al. 2011; Aumer et al. 2013; Okamoto 2013; Hopkins et al. 2014). Equipped with the same implementation of baryon physics as in the Illustris simulations, Marinacci, Pakmor & Springel (2014a) successfully produced MW-sized disc galaxies in a suite of zoom-in simulations. These simulations used the same initial conditions as the Aquarius Project (Springel et al. 2008), and the highest resolution hydrodynamical run (Aq-C-4) has sufficient resolution to identify and study the formation history and properties of the predicted dwarf galaxies.

In this work, we use both DM-only and hydrodynamical simulations of Aq-C-4 by Marinacci et al. (2014a) to study the impact of baryon processes on the halo/subhalo properties and the subhalo abundance. We will not limit our study to the bright satellites alone, i.e. those subhaloes containing stars, but we will also analyse the 'dark' ones. As it turns out, even the 'dark' subhaloes are systematically affected by baryonic processes in terms of their spatial distribution and mass functions.

This paper is organized as follows. In Section 2, we describe the numerical technique used in our simulations and the structure identification. The impact of baryons on the smooth DM distribution in the main halo and the global statistics of subhaloes are presented in Section 3. In Section 4, we investigate the impact of baryons on the total mass, the DM density profiles and $v_{\rm max}$ values of objects extracted from a matched subhalo catalogue of the DM and Hydro simulations. We aim to determine the main physical processes that shape the DM content in subhaloes by tracking the assembly history and evolution of bright satellites and 'dark' subhaloes. We discuss the implications of our study and its limitations in Section 5, and summarize our main findings in Section 6.

2 METHODS

2.1 The simulations

In this study, we use two cosmological simulations of an MW-sized halo, one being the full hydrodynamical Aq-C-4 run by Marinacci

et al. (2014a, referred to as 'Hydro' hereafter), and the other being a *control* DM-only simulation of the same halo (referred to as 'DMO' hereafter). This Aq-C halo was selected as a close match to the MW for the Aquila Comparison Project (Scannapieco et al. 2012), as well as several other studies (Wadepuhl & Springel 2011; Sawala, Scannapieco & White 2012; Okamoto 2013). The hydrodynamical Aq-C-4 simulation by Marinacci et al. (2014a) was performed with the moving mesh code AREPO (Springel 2010). The simulation adopted a physical model for galaxy formation and evolution developed by Vogelsberger et al. (2013), which includes SN feedback, metal enrichment and stellar mass return, AGN feedback (Di Matteo, Springel & Hernquist 2005; Springel, Di Matteo & Hernquist 2005a; Sijacki et al. 2007), and a spatially uniform, redshift-dependent ionizing background by Faucher-Giguère et al. (2009), which leads to complete reionization of neutral hydrogen by $z = 6$. Thermal feedback from SNe was implemented following a hybrid interstellar medium (ISM) model developed by Springel & Hernquist (2003), and galactic outflows were launched with a velocity scaled with the local DM velocity dispersion of the host halo, following a kinetic model similar to Okamoto et al. (2010) and Puchwein & Springel (2013).

The Aq-C-4 Hydro simulation has a mass resolution of 5.0×10^4 $M_\odot$ for gas and stars, and 3.0×10^5 $M_\odot$ for the DM component (see table 1 in Marinacci et al. 2014a), sufficient to simultaneously follow the main galaxy and its classical dwarf galaxies with a maximum circular velocity $v_{\rm max}$ between 12 and 24 $\rm km\,s^{-1}$ (Boylan-Kolchin et al. 2011). The gravitational softening length in the high-resolution region was kept fixed in comoving coordinates, corresponding to a physical length of 340 pc at $z = 0$. We re-run a DMO simulation of Aq-C-4 with the same numerical parameters controlling the force and time integration accuracy as used in Marinacci et al. (2014a). Thus, the effects of baryonic processes on the DM distribution can be well studied by comparing the DM simulation and its Hydro counterpart. At $z = 0$, the properties of the central galaxy of Aq-C-4 in the Hydro run are in very good agreement with those of a typical disc-dominated galaxy in terms of the mass budget in various components, the morphology, and the star formation history (Marinacci et al. 2014a). The properties of the diffuse gas and the metal distribution are also consistent with observations (Marinacci et al. 2014b). Moreover, we note that the robustness of the results was verified by a resolution study in Marinacci et al. (2014a).

2.2 Structure identification

To identify subhaloes both in the DMO and Hydro simulations, the snapshots were post-processed with the Amiga Halo Finder (AHF; Knollmann & Knebe 2009).[1] The AHF algorithm identifies structures based on density estimates calculated with an adaptive refinement technique, and naturally builds a halo–subhalo–subsubhalo hierarchy. The extent of a halo is determined by its density, $\bar{\rho}(r_{\rm vir}) = \Delta_{\rm vir}(z)\rho_{\rm bg}$, where $\bar{\rho}(r_{\rm vir})$ is the mean density within the virial radius $r_{\rm vir}$, $\rho_{\rm bg}$ is the background density, and $\Delta_{\rm vir}(z) = 178$ is the adopted virial overdensity.

AHF performs an iterative process to remove unbound particles until the final result converges to a set of bound particles within $r_{\rm vir}$. These sets of particles form the halo and subhaloes. The code then calculates various properties of the haloes and subhaloes, such as the mass in different components, the maximum value of the rotation curve $v_{\rm max}$, and the spin parameter. The results of AHF and other substructure finders such as SUBFIND (Springel et al. 2001) are generally in very good agreement (e.g. Onions et al. 2012; Pujol et al. 2014), and any residual differences are not expected to influence our results.

The IDs of collisionless particles are preserved in our simulations since there is no mass exchange between them. This allows us to construct subhalo merger trees using the built-in module MERGERTREE of AHF, which relies on tracking the membership of DM and star particles (identified by their IDs) within the different haloes and subhaloes. The merger trees are constructed for both the DM and Hydro simulations. For each halo/subhalo, we only consider the most massive progenitor in the previous snapshot as its parent. In addition, we only consider the haloes/subhaloes comprised of at least 10 particles. We have carefully checked the validity of the constructed merger trees by visually comparing the evolutionary paths of each individual object in terms of its position, velocity, and mass. There are rare cases when a subhalo is not detected by AHF in one snapshot output when the subhalo closely passes the centre of its host halo. These objects usually reappear in the next AHF catalogue if they have not been disrupted at pericentre. To avoid complications, we discard such subhaloes in this study.

With the MERGERTREE analysis package, we can also cross-match the $z = 0$ snapshots of the DM and Hydro simulations using the DM particles. We verify that this cross-match between the Hydro and DMO simulations is able to identify the 'same' objects by comparing their evolutionary paths. In Section 4.1, we show the orbital and mass growth histories of several of these matched objects. We note however that substantial orbital phase offsets are expected to appear in most pairs due to the inclusion of baryonic processes; thus, the positions of the subhaloes in the two simulations are not expected to exactly match each other. Also, some haloes/subhaloes identified in the DMO simulation do not have counterparts in the Hydro simulation, given that substructures are destroyed at a higher rate in the latter run.

3 BARYONIC IMPACT ON THE PROPERTIES OF THE MAIN GALAXY AND ITS SATELLITES

One of the goals of this study is to identify the main physical processes shaping the distribution of DM in the main galaxy and its substructures. In this section, we focus on important galaxy properties such as the spatial distribution, abundance, and mass function of satellites, as well as the DM density profiles in the DMO and Hydro simulations.

3.1 Spatial distribution and abundance of subhaloes

In Fig. 1, we show projected DM density maps at $z = 0$ for a slice of thickness $250\,h^{-1}$ kpc centred on the MW-sized halo for the DMO (top panel) and the Hydro (bottom panel) simulations, respectively. Numerous substructures are clearly visible in both simulations. Despite the overall similarity in the morphology and size of the main halo between the two simulations, there are notable differences in the abundance and spatial distribution of the subhaloes, especially in the central region, as demonstrated in Fig. 2, which shows the positions of all the DM subhaloes and bright satellites (subhaloes that contain stars) within the virial radius of the main galaxy at the present epoch. It is clear that there are fewer subhaloes in the Hydro

[1] The code is available at http://popia.ft.uam.es/AHF/Download.html. In this study, we use the version ahf-v1.0-084. It also contains an analysis tool called MERGERTREE, which we have used to construct the merger tree and to cross-match the subhaloes between the DMO and Hydro simulations.

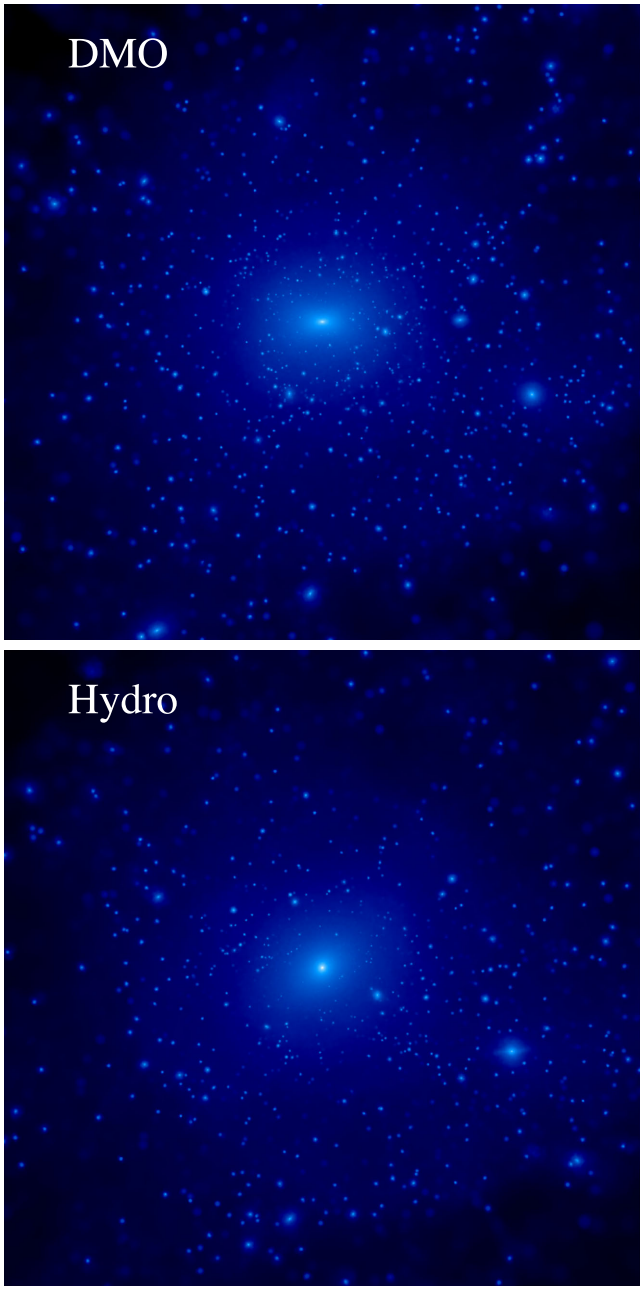

Figure 1. Projected DM density maps within a $250\,h^{-1}$ kpc slice centred on the main halo at redshift $z = 0$ in the DMO (top panel) and Hydro (bottom panel) simulations, respectively. The size of the displayed region is $0.7\,h^{-1}$ Mpc on a side.

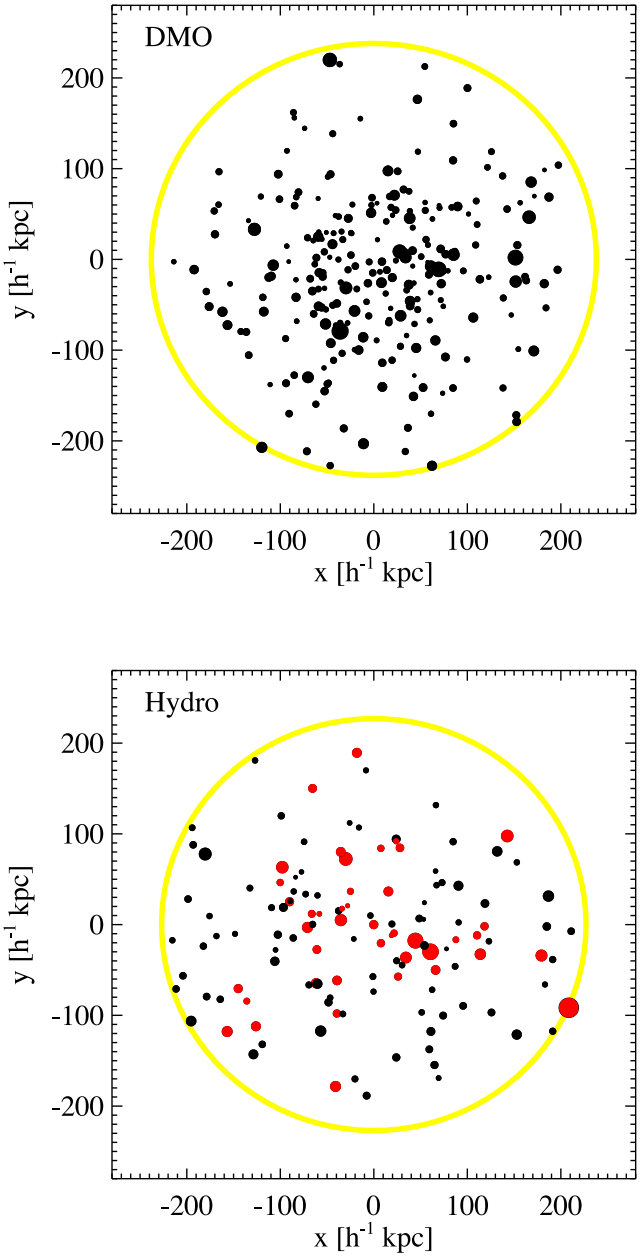

Figure 2. The spatial distribution of subhaloes at redshift $z = 0$ in the DMO (top panel) and Hydro (bottom panel) simulations, respectively. The black filled circles represent DM subhaloes, while the red filled circles represent bright satellites which have formed stars. The size of the symbols is scaled with the subhalo mass. The solid yellow circle indicates the virial radius calculated by AHF (with overdensity $\Delta_{\rm vir} = 178$). The Hydro simulation produces fewer subhaloes than the DMO counterpart, with a pronounced depletion of low-mass subhaloes near the central region. The bright satellites are only a small fraction of the entire subhalo population.

simulation than in the DMO one; in particular, the large number of low-mass subhaloes found in the DMO simulation is clearly reduced in the Hydro case. Moreover, it is seen that only a fraction of the subhaloes presented in the DMO simulation can be found in the Hydro simulation. Note that not necessarily the most massive ones are able to host bright satellites that form stars.

To quantify the spatial distribution of subhaloes, we compare the radial number density of subhaloes in different mass ranges from both the DMO and Hydro simulations in Fig. 3. It has been shown that in *N*-body simulations the spatial distribution of subhaloes follows a universal function which is less concentrated than the density profiles of DM haloes. It can be parametrized by the Einasto profile (Gao et al. 2012)

$$n(r)/\langle n\rangle_{\rm DMO} = \langle n\rangle_{-2,0} \exp\left\{-\frac{2}{\alpha}\left[\left(\frac{r}{r_{-2}}\right)^{\alpha} - 1\right]\right\}. \quad (1)$$

We fit our data with the Einasto profile for subhaloes in two mass ranges, delineated by maximum circular velocities $v_{\rm max} > 5$ km s^{-1} and $v_{\rm max} > 10$ km s^{-1} as shown in Fig. 3. The radial abundance of subhaloes in the Hydro simulation is consistently lower than that in the DMO one, and the effect increases towards the centre

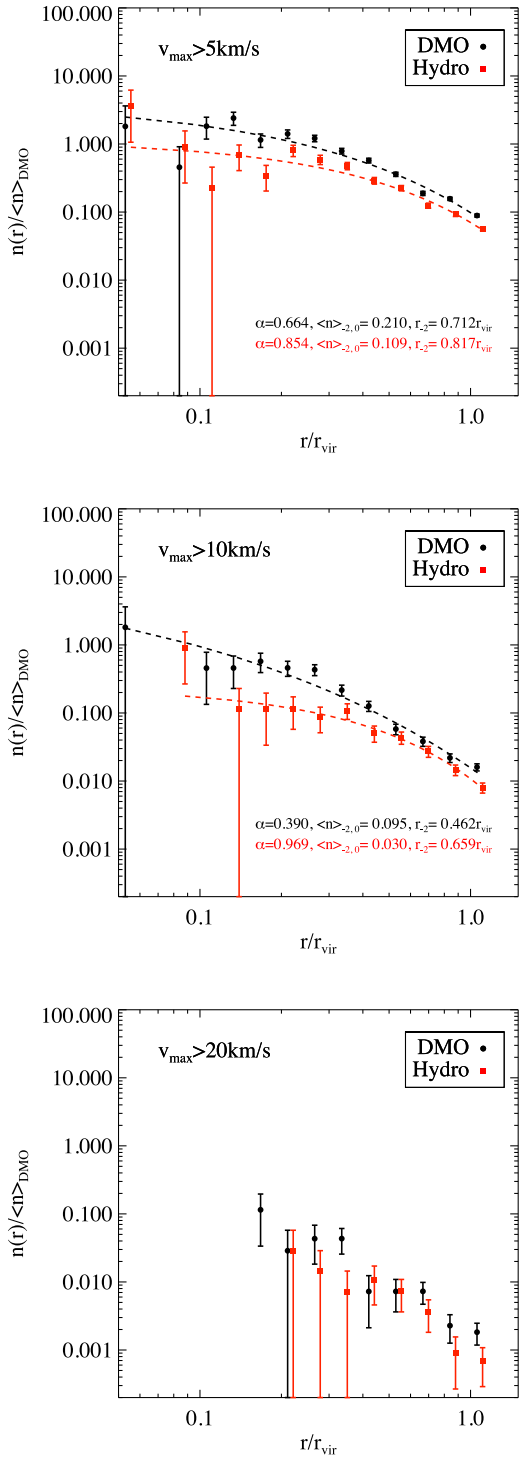

Figure 3. The number density of subhaloes in different mass ranges as a function of distance to the centre of the main halo, both for the DMO (black symbols) and Hydro (red symbols) simulations. The distance r is normalized to the virial radius of the main halo, while the subhalo abundance is normalized to $\langle n \rangle_{\rm DMO}$, the total number of DM subhaloes identified in the DMO simulation divided by the entire volume enclosed by $r_{\rm vir}$. The top, middle, and bottom panels show subhaloes in three different mass ranges, as indicated by the maximum circular velocity $v_{\rm max} > 5$ km s^{-1}, $v_{\rm max} > 10$ km s^{-1}, and $v_{\rm max} > 20$ km s^{-1}, respectively. The error bars are computed using the Poisson error $\sqrt{N_r}$, where N_r is the number of subhaloes within each radial bin. The dashed lines are fits to the Einasto profile, as given by equation (1).

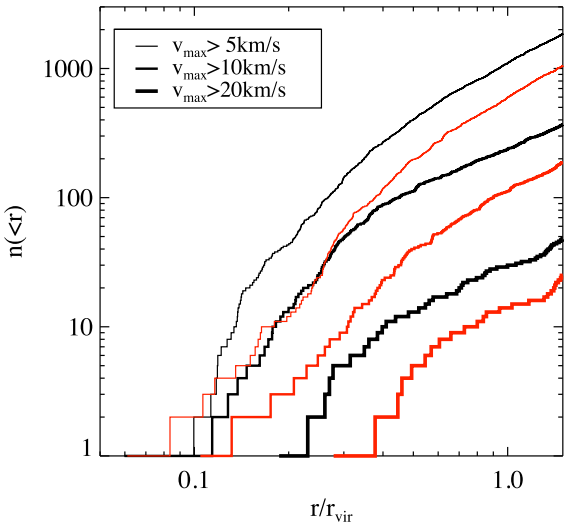

Figure 4. The cumulative number of subhaloes in different mass ranges as a function of distance to the centre of the main halo, both for the DMO (black lines) and Hydro simulations (red lines). The three mass ranges are the same as in Fig. 3: $v_{\rm max} > 5$ km s^{-1}, $v_{\rm max} > 10$ km s^{-1}, and $v_{\rm max} > 20$ km s^{-1}, respectively.

for the most massive subhaloes. There are not enough data points within $0.2r_{\rm vir}$ for $v_{\rm max} > 20$ km s^{-1} to perform reliable fitting with an Einasto profile. The cumulative radial distribution of subhaloes in Fig. 4 confirms this trend. The total number of subhaloes at any given radius, with the exception of the innermost regions ($r/r_{\rm vir} \lesssim 0.1$) in the $v_{\rm max} > 5$ km s^{-1} cut, is consistently lower in the Hydro simulation than in the DMO run, and this is particularly evident for the most massive subhaloes in the central regions.

Both Figs 3 and 4 suggest that subhaloes are subject to being disrupted more easily in the Hydro simulation. A similar radial distribution can also be found in D'Onghia et al. (2010a) and Yurin & Springel (2015), in which it was suggested that the reduction of subhaloes was due to enhanced tidal effects and accelerated disruption rates from a combination of DM contraction and the presence of the stellar disc. In addition, enhanced dynamical friction from the adiabatically contracted DM distribution of the main halo would cause the subhaloes to sink more rapidly. The combination of these factors results in fewer massive subhaloes in the central region in the Hydro simulation than in the DMO one. We will address the impact of the central galaxy on the abundance of its satellites in Section 4.

A comparison of the cumulative distribution of DM subhaloes between the DMO and Hydro simulations is shown in Fig. 5. Both simulations show a power-law distribution of the subhalo abundance, $N(>v_{\rm max}) \propto v_{\rm max}^{-3}$ in terms of maximum circular velocity, and $N(>M_{\rm sub}) \propto M_{\rm sub}^{-1}$ in terms of mass, similar to the relations reported for DM subhaloes based on the Aquarius simulations (Springel et al. 2008) and the Phoenix simulations (Gao et al. 2012). The slopes of both distribution functions are similar in our DMO and Hydro simulations. However, the total number of subhaloes in the Hydro simulation is consistently lower by ∼50 per cent than in the DMO case, except for the range where $v_{\rm max} > 35$ km s^{-1} (or equivalently $M_{\rm sub} > 4 \times 10^9$ M$_\odot$ in terms of mass).

The bright satellites, which are here defined as subhaloes containing stars in the Hydro simulation, show a different distribution from the DM subhaloes at a critical point of $v_{\rm max} \sim 20$ km s^{-1} (corresponding to a mass of $M_{\rm sub} \sim 10^9$ M$_\odot$). At the low-mass

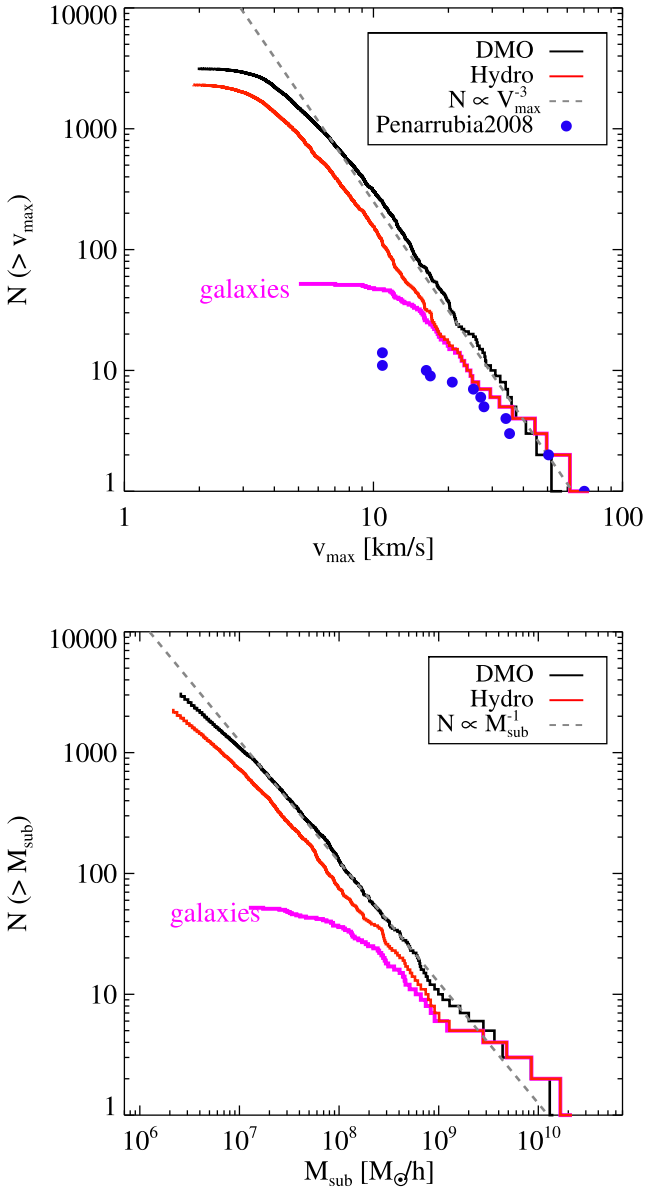

Figure 5. The cumulative distribution of the number of subhaloes from the DMO (black solid line) and Hydro (red solid line) simulations, as a function of the maximum circular velocity $v_{\rm max}$ (top panel) and the subhalo mass $M_{\rm sub}$ (bottom panel). The grey dashed lines are fits from the literature, $N(>v_{\rm max}) \propto v_{\rm max}^{-3}$ (top panel), or $N(>M_{\rm sub}) \propto M_{\rm sub}^{-1}$ (bottom panel). Bright satellites (subhaloes that have stars) are represented by the pink solid curve, while observations by Peñarrubia et al. (2008a) are shown with blue dots, for comparison.

end, the probability of a subhalo hosting stars steadily decreases as $v_{\rm max}$ decreases. The 'missing satellite problem' appears clearly striking if we simply compare the number of DM subhaloes at $v_{\rm max} < 10\,{\rm km\,s^{-1}}$ with observations of Peñarrubia, McConnachie & Navarro (2008a), because the former is more than two orders of magnitude higher. However, the number of satellites (i.e. subhaloes with stars) is much closer to the observations, and the discrepancy between the two becomes even smaller when detection and completeness limits of current surveys are accounted for.

At the massive end, $v_{\rm max} > 20\,{\rm km\,s^{-1}}$, the number of bright satellites agrees well with observations and it matches that of DM subhaloes. The value of $v_{\rm max} \sim 20\,{\rm km\,s^{-1}}$ marks a transition in dwarf galaxy formation shaped by reionization, similar to previous studies (Okamoto, Gao & Theuns 2008; Okamoto & Frenk 2009). The total number of massive dwarf galaxies with $v_{\rm max} > 30\,{\rm km\,s^{-1}}$ within the virial radius $r_{\rm vir}$ of the central galaxy is 6 in our Hydro simulation, which is almost half the value (11) of massive subhaloes found in the DMO simulation. Note that this corresponds to the mass range of the 'massive failures' considered in Boylan-Kolchin et al. (2011, 2012). Still, our result is slightly higher than the total number (4) of massive satellites in the MW, including Large Magellanic Cloud and Small Magellanic Cloud, which have $v_{\rm max}$ above $30\,{\rm km\,s^{-1}}$ (Peñarrubia et al. 2008a). Moreover, detailed variations from one main galaxy to another could, in principle, resolve the residual discrepancy.

The sharp contrast in the number of dwarf galaxies between the DMO and Hydro simulations highlights the critical role of baryonic physics in galaxy formation, and it points to a potentially viable solution of the 'missing satellite' and the 'too big to fail' problems, in agreement with suggestions by some previous studies (e.g. Brooks et al. 2013; Sawala et al. 2014; Mollitor, Nezri & Teyssier 2015).

3.2 Mass functions of subhaloes

In order to investigate effects of baryons on the subhalo mass, in Fig. 6 we compare the subhalo mass $M_{\rm sub}$ (top panel) and the maximum circular velocity $v_{\rm max}$ (bottom panel) at $z = 0$ of the matched pairs between the two simulations. As the fitting curve (black solid line) is below the diagonal dashed line ($M_{\rm sub}$(Hydro) = $M_{\rm sub}$(DMO), or $v_{\rm max}$(Hydro) = $v_{\rm max}$(DMO)), it is clearly seen that the majority of subhaloes in the Hydro simulation are less massive than their counterparts in the DMO simulation, similar to the subhalo abundance findings in Section 3.1. The subhalo mass function of the Hydro simulation peaks at $\sim 5 \times 10^6\ h^{-1}\,{\rm M}_\odot$, which is about a factor of 2 lower than the peak of the DMO subhalo mass function at $\sim 10^7\ h^{-1}\,{\rm M}_\odot$.

In the Hydro simulation, only massive subhaloes can form stars. The minimum mass for subhaloes to host star formation is log ($M_{\rm sub}$) = 7.5 (or $v_{\rm max} = 10\,{\rm km\,s^{-1}}$), although it may be affected by the resolution of the simulation. In the mass range between 10^8 and $10^9\ h^{-1}\,{\rm M}_\odot$ where we have sufficient mass and spatial resolution, there is a mixture of 'dark' subhaloes and bright satellites (subhaloes that contain stars). Such a co-existence of dark subhaloes and bright satellites implies that a linear $M_{\rm halo}$-M_* correlation, as commonly assumed in semi-analytical galaxy models and abundance matching techniques (e.g. Guo et al. 2010; Moster, Naab & White 2013), may not hold in the dwarf galaxy regimes, since some massive haloes do not host galaxies with stars. This would complicate the application of the abundance matching to dwarf galaxies (Garrison-Kimmel et al. 2014a; Guo & White 2014) and the assignment of galaxies to DM haloes in N-body simulations.

Another important parameter is the peak mass of each subhalo, $M_{\rm peak}$, defined as the maximum mass attained by the progenitor before it was accreted by its host. Using the peak mass is currently the standard method in abundance matching or semi-analytical modelling when dealing with subhaloes (e.g. Garrison-Kimmel et al. 2014a; Guo & White 2014), since this quantity represents a physical state unmodified by the subsequent interaction between the subhalo and the host. Fig. 7 shows a comparison of $M_{\rm peak}$ from the DMO and Hydro simulations. We find that subhaloes below $10^9\ h^{-1}\,{\rm M}_\odot$ generally have lower $M_{\rm peak}$ in the Hydro simulation than in the DMO simulation, and that subhaloes with peak mass higher than $10^9\ h^{-1}\,{\rm M}_\odot$ are able to form stars. However, there are a few 'outliers': two subhaloes with peak mass above $10^9\ h^{-1}\,{\rm M}_\odot$

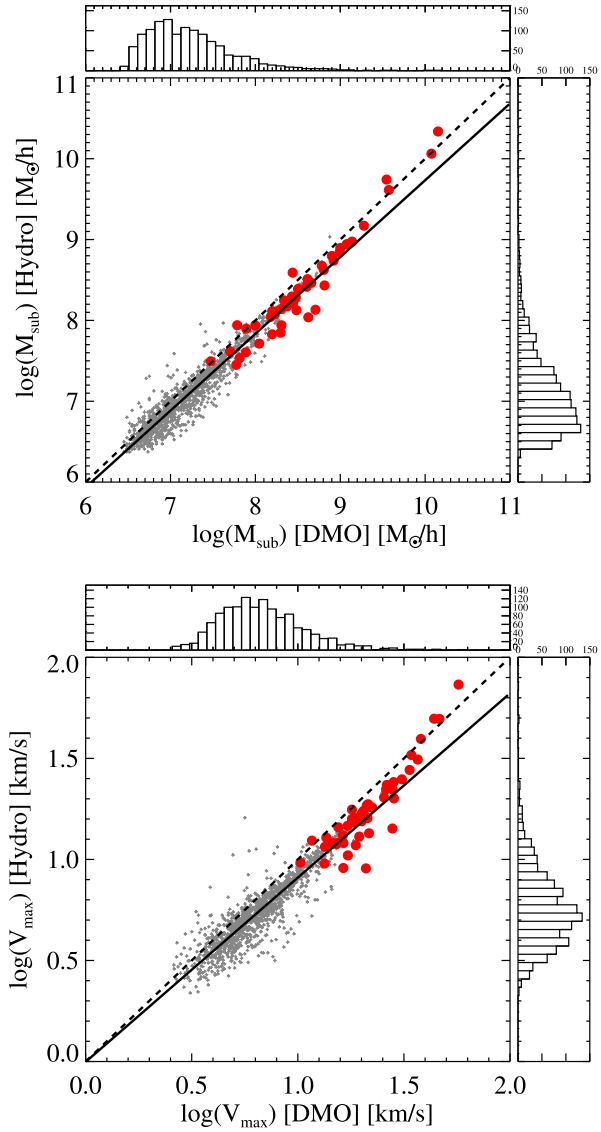

Figure 6. Comparison of subhalo properties of the matched pairs at $z = 0$ in both the DMO and Hydro simulations. The top panel shows the subhalo mass $M_{\rm sub}$ distribution function, while the bottom panel shows the maximum circular velocity $v_{\rm max}$ distribution function. The grey dots represent all dark subhaloes (subhaloes that did not form stars), while the filled red circles represent bright satellites (subhaloes that contain stars). The solid black line is the fitting curve for all the subhaloes (including both dark and star-forming ones), while the dashed line indicates $M_{\rm sub}$(Hydro) = $M_{\rm sub}$(DMO) in the top panel, and $v_{\rm max}$(Hydro) = $v_{\rm max}$(DMO) in the bottom panel.

remain completely dark, while three subhaloes with peak mass below $10^9\ h^{-1}\,{\rm M}_\odot$ actually contain stars. The fitting of the data shows that

$$\log M_{\rm peak}[{\rm Hydro}] = 1.10 \log M_{\rm peak}[{\rm DMO}] - 1.05, \qquad (2)$$

which means that the subhalo peak mass is ∼30 per cent lower in the Hydro simulation than in the DMO simulation for $M_{\rm peak} \sim 10^9\ h^{-1}\,{\rm M}_\odot$ and ∼44 per cent lower for $M_{\rm peak} \sim 10^8\ h^{-1}\,{\rm M}_\odot$.

Our results suggest that the impact of hydrodynamics on the halo mass could be easily amplified in the early growth stages when the haloes increase their mass exponentially (Bosch et al. 2014; Correa et al. 2015), and that the assumption of a monotonic relation between stellar mass of a galaxy and its peak mass in the abundance matching technique is not valid. Hydrodynamic simulations should hence be employed for a more reliable study of the properties of dwarf galaxies, also as suggested by previous work (e.g. Sawala et al. 2014; Velliscig et al. 2014).

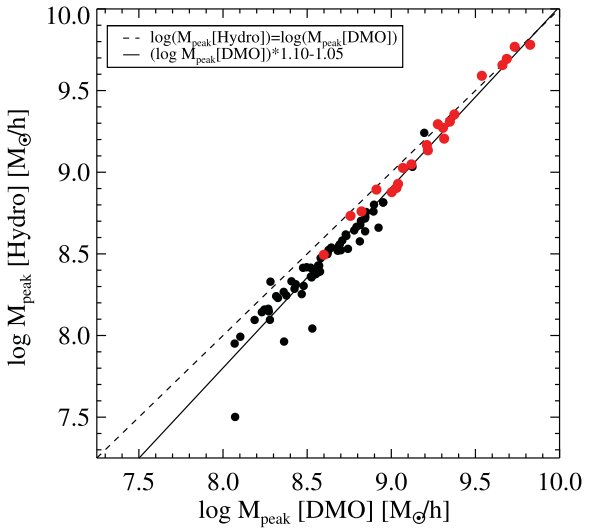

Figure 7. A comparison of the subhalo peak mass $M_{\rm peak}$ (the maximum mass attained by the progenitor before it was accreted by its host) of matched pairs in both the DMO and Hydro simulations. The black filled circles are the 'dark' subhaloes and the red filled circles represent bright satellites. The black solid line is the fitting curve of all subhaloes, while the dashed line indicates $M_{\rm peak}$(Hydro) = $M_{\rm peak}$(DMO).

3.3 DM distribution and density profile of the main host

To study the effects of baryons on the DM distribution of the main host, we compare the DM shape and density profile of the main host in both simulations. We apply a principal component analysis to the DM halo and compute the three axis parameters a, b, and c based on the eigenvalues of the moment of inertia tensor for all the DM particles within a given shell (following the method by Zemp et al. 2011). The halo shape can be quantified by the intermediate-to-major axis ratio, b/a, and the minor-to-major axis ratio, c/a, as shown in Fig. 8 (top panel), which compares the axial ratios at different distances from the galactic centre in both the DMO and Hydro simulations. The shape of the DM halo differs significantly between the two simulations. In the inner region within $10\,h^{-1}$ kpc, it is triaxial with the triaxiality parameter (defined as $T = [a^2 - b^2]/[a^2 - c^2]$ as in Zemp et al. 2011) $T \sim 0.9$ in the DMO simulation, but in the Hydro simulation it is close to an oblate spheroid with $b/a \sim 1$ and $c/a > 0.7$. The difference in halo shape between the DMO and Hydro simulations continues towards larger galactic distance out to ∼100 h^{-1} kpc, but they converge at the virial radius $r \sim 200\ h^{-1}$ kpc. These results are in good agreement with previous studies (Springel, White & Hernquist 2004; D'Onghia et al. 2010a; Vera-Ciro et al. 2011; Zemp et al. 2011; Bryan et al. 2013), and demonstrate that the impact of baryons on the DM halo shape is significant up to the virial radius, a spatial scale much larger than that of the stellar disc or the central galaxy. We note that a similar effect is seen in gas-rich mergers of galaxies, where gas inflows (Barnes & Hernquist 1991) and nuclear starbursts (Mihos & Hernquist 1996) can significantly modify the shapes and orbital properties of remnants (Barnes & Hernquist 1996).

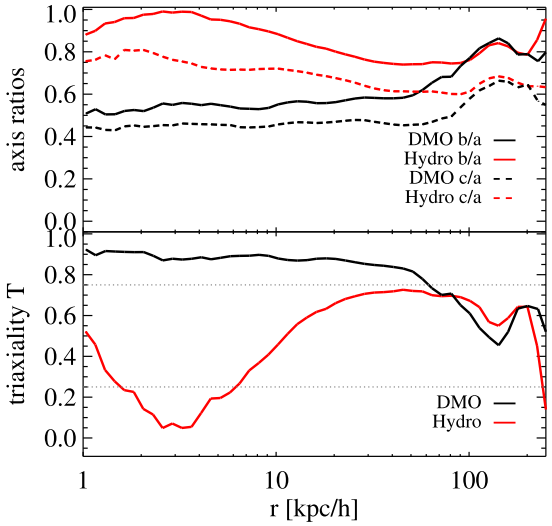

Figure 8. Comparison of the shape of the main DM halo from the DMO (in black) and Hydro (in red) simulations. Top panel: the intermediate-to-major axis ratio b/a (solid lines) and the minor-to-major axis ratio c/a (dashed lines) as a function of distance to the galactic centre. Bottom panel: the triaxiality T, defined as $T = (a^2 - b^2)/(a^2 - c^2)$, of the main DM halo as a function of galactic radius. The dotted lines indicate $T = 0.25$ and 0.75, marking the transitions from oblate/prolate to triaxial halo shapes. The plot shows that in the inner region the DM halo is more spheroidal in the Hydro simulation, but it is triaxial in the DMO simulation.

In addition to the halo shape, remarkable differences between the Hydro and DMO simulations are also present in the DM density profile of the main host. Adiabatic contraction of the DM distribution by baryonic processes is a well-known effect. Historically, adiabatic contraction effects were calculated analytically based on the assumption of circular orbits and conservation of angular momentum. Gnedin et al. (2004) refined the calculation by considering the eccentricities of the orbits in a more realistic cosmological context. Even with such a modification, the density profile of DM in the inner region could be overestimated without the inclusion of more baryon physics other than cooling and star formation. Recently, Marinacci et al. (2014a) showed that an enhancement of the DM density in the inner region was present for most of the eight MW-sized haloes studied in their simulations (however at a lower resolution than that used here).

To illustrate the effect of adiabatic contraction on the DM distribution, we present in Fig. 9 the spherically averaged DM density profile of the main halo both from the DMO and Hydro simulations (top panel), as well as a comparison with the adiabatic contraction calculation (bottom panel) based on the DMO density profile using the CONTRA[2] code (Gnedin et al. 2004, 2011). This code calculates the response of a DM distribution to the condensation of baryons. We input the DM distribution at $z = 0$ from the DMO simulation as the state before contraction, and the baryonic mass distribution at $z = 0$ from the Hydro simulation as the source of adiabatic contraction. Since the contraction of DM is naturally followed in the Hydro simulation, we can compare the DM density profile from the Hydro simulation with the theoretical expectation from CONTRA. The lower panel of Fig. 9 shows the expected enhancement of DM from the DMO simulation (dash–dotted line) as if it would host the same galaxy produced by the Hydro simulation. The red solid

[2] http://dept.astro.lsa.umich.edu/~ognedin/contra

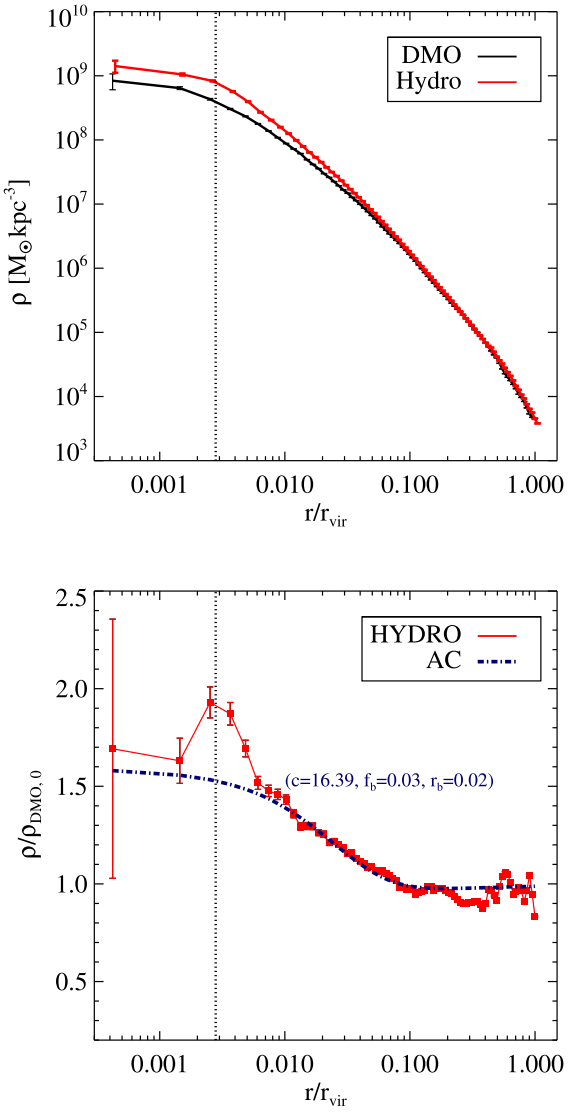

Figure 9. Comparison of the radial DM density profile of the main halo in our different simulations. Top panel: the halo DM density profiles from the DMO (black solid curve) and Hydro (red solid curve) simulations, respectively. A factor of $\frac{\Omega_m - \Omega_b}{\Omega_m}$ is applied to the density profile from the DMO simulation. Bottom panel: the enhancement of DM from the Hydro simulation (red solid curve) in comparison with the adiabatic contraction calculation (blue dash–dotted curve) based on the DMO density profile using the CONTRA code (Gnedin et al. 2011). The error bars are based on the Poisson error $\sqrt{N}$, where N is the number of DM particles in each radial bin. The vertical dotted line in both plots marks the position at which the gravity force equals its exact Newtonian form, $r = 2.8\,\epsilon$, where ϵ is the gravitational softening length. An enhancement of the DM concentration due to adiabatic contraction is present in the Hydro simulation in the inner region up to $r \sim 0.1 r_{\rm vir}$.

symbols show the DM density profile measured in the Hydro simulation. This plot shows a significant enhancement of the DM in the inner region out to $r \sim 0.1\,r_{\rm vir}$ in the Hydro simulation, which is consistent with the expected adiabatic contraction. Interestingly, in the very central region, we see more DM enhancement in the Hydro simulation compared to the result from CONTRA. While it is possible that the DM distribution in the Hydro simulation follows a much more complex evolution than the simplified analytical calculation in CONTRA, we also note that the 'bump' in the lower panel of Fig. 9

may be subject to numerical uncertainty as it occurs on a scale very close to the spatial resolution of the simulations.

In our Hydro simulation, the response of DM due to gas cooling and condensation is consistent with the expectation of adiabatic contraction. As demonstrated in Marinacci et al. (2014a), this holds true for the majority of the MW-sized haloes in the hydrodynamic simulations. The agreement between our simulation and CONTRA fitting suggests that the latter provides a good description of the DM distribution in $L_\star$ galaxies. Since CONTRA has been calibrated using a suite of different hydrodynamic simulations (Gnedin et al. 2011), the agreement between our result and CONTRA therefore reflects a consistent response of DM with respect to gas cooling and condensation, despite substantial differences in how feedback was modelled.

Interestingly, no DM core is formed in our simulated halo. We note that recent simulations of haloes more massive than 10^{12} $M_\odot$ by Macciò et al. (2012) and Mollitor et al. (2015) show flattened DM distributions within the inner 5 kpc. Compared to our simulations, these studies employed a different feedback model featuring a more bursty stellar feedback. While feedback processes such as energy and momentum from SN explosions may hence change the contraction of DM in the central region, such effects sensitively depend also on how the feedback injection is modelled in detail.

3.4 DM distributions and density profiles of subhaloes

Similar to the main halo, we identify subhaloes in both the DMO and Hydro simulations using the AHF group finder. We first locate the centre of mass from the output of AHF for each matched object, then compute the spherically averaged density for DM particles of each subhalo based on the particle locations in the original snapshot. Fig. 10 shows the DM density profiles of six matched subhaloes at $z = 0$ from both simulations, as well as the corresponding circular velocity curves. These subhaloes cover a wide range of total mass, from massive bright dwarf galaxies to 'dark' subhaloes. The circular velocity of each subhalo is calculated as $\sqrt{GM(<r)/r}$, where $M(<r)$ is the enclosed mass within r. We further compute the contributions from DM and baryonic components to the rotation curve in order to determine whether the differences in $v_{\rm max}$ from the two simulations are due to highly concentrated baryons or a genuine response of DM to baryonic processes. For the DMO simulation, we assume that the distribution of baryons follows that of the DM but differs in mass by a factor of $\Omega_{\rm b}/\Omega_{\rm m}$. We note, however, that the most massive subhalo, sub 10, contains more baryonic mass in the Hydro simulation than in the DMO simulation, while the least massive subhaloes (such as sub 162 and sub 244) contain much less baryonic mass in the Hydro simulation than expected based on the DMO simulation.

From Fig. 10, the computed density profiles of the subhaloes from the Hydro simulation match their counterparts from the DMO simulation quite closely. However, the local distribution of DM is better probed by the rotation curves as they depend sensitively on the mass enclosed within a certain radius. As shown in the right-hand panels of Fig. 10, significant differences are evident between the rotation curves from these two simulations, in particular with respect to the contribution of DM as represented by the solid curves. For the first three subhaloes (sub 10, 19, and 43), the contribution from the DM in the Hydro simulation is higher than that in the DMO simulation. They contain slightly more DM in the Hydro simulation than in the DMO one, showing some mild contraction. In addition, the amount of contraction in these three subhaloes varies with their total mass, with sub 10 showing the strongest contraction and sub

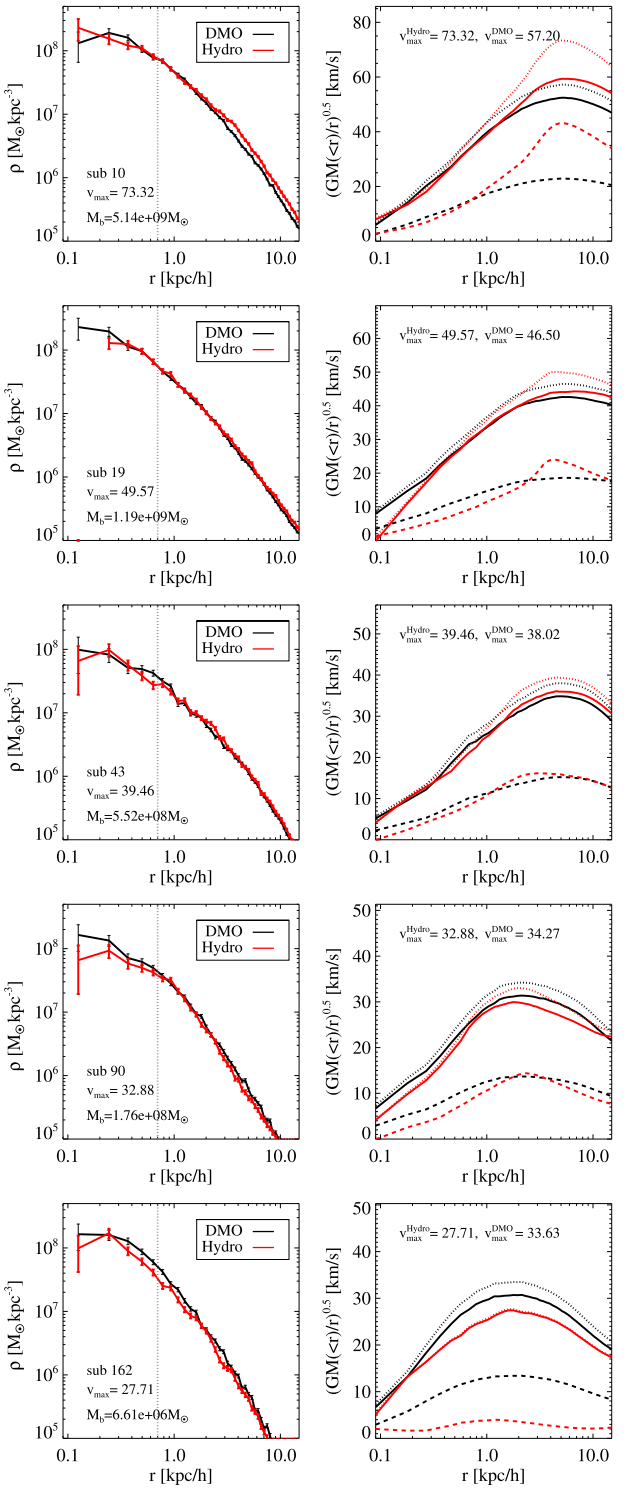

Figure 10. A comparison of the DM density profiles (left column) and the circular velocity curves (right column) of six matched subhaloes from the DMO (in black) and Hydro (in red) simulations. As in Fig. 9, the DMO density profiles are multiplied by a factor of $\frac{\Omega_{\rm m}-\Omega_{\rm b}}{\Omega_{\rm m}}$, and the dashed vertical line indicates $r = 2.8\,\epsilon$. For each subhalo, its ID, $v_{\rm max}$, and baryonic mass $M_{\rm b}$ are listed. In the right-hand panels, the total circular velocity, and contributions from the DM and baryons are represented by the dotted, solid, and dashed curves, respectively. The distribution of baryons in the DMO simulation is assumed to follow that of the DM multiplied by a factor of $\Omega_{\rm b}/\Omega_{\rm m}$.

43 the weakest. On the other hand, the other three subhaloes, sub 90, 162, and 244, show slightly reduced DM concentrations in the Hydro simulation compared with the DMO one.

In the inner region, we have not found clear signs of DM cores in these subhaloes. However, the absence of DM cores could potentially be due to a limited mass and spatial resolution of the simulations. The gravitational softening length in our simulations is a factor of 2–3 larger than in the most recent high-resolution simulations focusing on (isolated) dwarf galaxies (Governato et al. 2012; Teyssier et al. 2013; Madau et al. 2014; Oñorbe et al. 2015).

4 THE IMPACT OF BARYONS ON THE EVOLUTION OF SUBHALOES

4.1 Importance of individual physical processes

Baryonic processes play a critical role in the formation and evolution of galaxies. In this study, we focus on three major mechanisms related to baryons that impact the mass distribution in galaxies: adiabatic contraction, reionization, and tidal disruption. Adiabatic contraction due to gas cooling and condensation leads to an increase of the density in the galaxy centre. Reionization not only ionizes and evaporates gas from galaxies, but can also prevent gas accretion from the intergalactic medium (IGM). Tidal truncation from gravitational interactions can result in the removal and redistribution of both dark and baryonic matter components.

The relative impact of these processes on galaxy properties and their evolution depends on the galaxy mass. Based on the properties found in Section 3, the subhaloes in our simulations can be categorized into three main groups according to their $v_{\rm max}$ (or alternatively mass) at $z = 0$. The first group consists of massive subhaloes with $v_{\rm max} > 35\,{\rm km\,s^{-1}}$ ($M_{\rm sub} > 4 \times 10^9\ {\rm M}_\odot$), where adiabatic contraction tends to increase the amount of DM within the virial radius. These subhaloes usually form stars and are therefore 'bright'. The second group are the least massive ones with $v_{\rm max} < 20\,{\rm km\,s^{-1}}$ ($M_{\rm sub} < 10^9\ {\rm M}_\odot$), and are mostly 'dark' with little or no star formation. These small subhaloes are affected by reionization. The third group are subhaloes with intermediate masses with $v_{\rm max} \sim 20$–$35\,{\rm km\,s^{-1}}$. These subhaloes show signs of a competition between adiabatic contraction and tidal disruption. While adiabatic contraction is able to increase the $v_{\rm max}$ of these subhaloes, they often suffer from strong tidal effects in the Hydro simulation that remove both DM and baryonic mass, thus effectively reducing $v_{\rm max}$ once they are close enough to the central galaxy. In what follows, we will show some examples of these evolutionary paths.

4.1.1 The role of adiabatic contraction

As we have seen from Fig. 10, three subhaloes (sub 10, 19, and 43) show signs of contracted DM in the Hydro simulation. Subhalo 10 is the most massive among them, with $v_{\rm max} = 73\ {\rm km\,s^{-1}}$ (in the Hydro simulation). Fig. 11 shows the assembly history and dynamical evolution of sub 10. Not surprisingly, this object is able to fuel star formation continuously from high redshift to the present day, as shown by the 'blue' stars in the composite images of the figure. Both the Hydro and DMO simulations produce similar trajectories for sub 10, which is simply a single fly-by at $z \sim 0.3$. A slight reduction of the total mass and $v_{\rm max}$ is evident in both simulations due to this fly-by; but overall, the effect of baryons on this object is dominated by adiabatic contraction, making it more resilient to disruption. It builds up mass steadily, and it reaches a total mass of $2.1 \times 10^{10}\ h^{-1}\,{\rm M}_\odot$ at $z = 0$ in the Hydro simulation, about 50 per cent more massive than its counterpart in the DMO simulation. It is interesting to note that the $v_{\rm max}$ of sub 10 in the Hydro simulation is substantially larger than that in the DMO simulation throughout the time despite that its total mass is almost identical in the two runs. This suggests that the contraction of DM within sub 10 has been established at an early stage if adiabatic contraction is indeed responsible for the enhanced DM density profile shown in the top panel of Fig. 10. Moreover, in the Hydro simulation, there is a non-negligible contribution of the baryons to the total gravitational potential of sub 10 in the inner regions which also helps explaining the different values of $v_{\rm max}$ (see Fig. 12).

To demonstrate the effect of adiabatic contraction in subhaloes, Fig. 12 shows a comparison of the radially enclosed DM mass of sub 10 from both Hydro and DMO simulations against prediction from the CONTRA code (top panel), and its evolution from the DMO simulation (bottom panel). In the inner region between 1 and 4 kpc, the Hydro simulation and the CONTRA calculation show similar enhancements of the enclosed DM mass by ∼25 per cent due to baryons. Beyond 4 kpc, the enclosed DM mass in the Hydro simulation is consistently higher than the expectation from CONTRA.

We find that the discrepancy between the Hydro and DMO simulations is mostly due to tidal removal of the loosely bound material in the outer parts of sub 10 in the DMO simulation, as evidenced by the change of radial enclosed DM mass with time in Fig. 12 (bottom panel). Sub 10 experiences continuous mass-loss in the outer region after the pericentric passage at redshift $z = 0.10$. Although mass-loss also occurs in sub 10 in the Hydro simulation, as shown in the mass evolution in Fig. 11, the amount is much smaller than that in the DMO simulation. These results show that when baryonic effects are included, massive systems similar to sub 10 become more resilient to tidal disruption since adiabatic contraction and the presence of baryons in the inner regions tend to increase the binding energy.

Similar effects of adiabatic contraction could also help explain the survival of the bright satellites of galaxy clusters reported for the Illustris simulation (Vogelsberger et al. 2014c). It was found that those galaxies (with stellar mass $\sim 10^{10}\ h^{-1}\,{\rm M}_\odot$, much more massive than sub 10, the largest dwarf in our simulation) are more resilient to tidal disruption in the central cluster regions than satellites in pure *N*-body simulations due to the increased concentration of DM and stellar components, in agreement with our findings in this study.

The role of adiabatic contraction becomes progressively less important for lower mass DM haloes/subhaloes, as we have shown in Fig. 10. In particular, for subhaloes with $v_{\rm max} < 35\ {\rm km\,s^{-1}}$, the total amount of baryons (mostly in the form of cool gas and stars) no longer plays a substantial gravitational role in these systems. We also note that our simulations include only a few massive subhaloes, so that some scatter in their properties is inevitable. A more accurate estimate of the galaxy mass at which adiabatic contraction turns ineffective will require a much larger sample of (massive) subhaloes than the one analysed in this study.

4.1.2 The role of reionization

The epoch of reionization is an important landmark event in cosmic history during which photons from young stars or accreting black holes ionize the neutral hydrogen. The latest results of *Planck* (Planck Collaboration XIII 2015) indicate that the Universe was 50 per cent reionized at $z \approx 9$, while Gunn–Peterson absorption

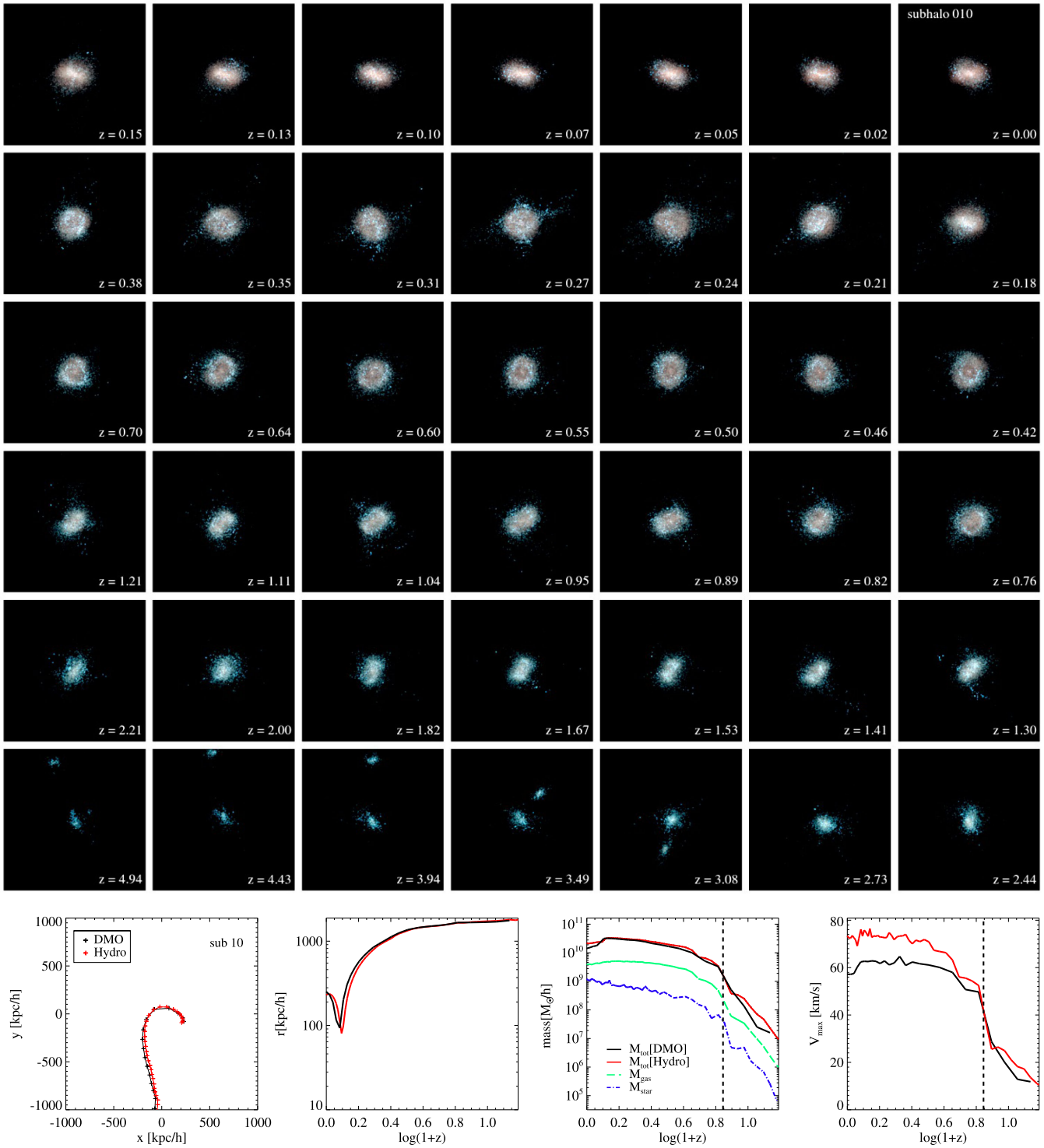

Figure 11. Time evolution of the most massive subhalo (sub 10) in the simulations. Top panels: projected density map of the stellar component from redshift $z \sim 5$ to $z = 0$. The composite images have used RGB colours mapped from the *K*, *B*, and *U* bands, respectively. The lower panels show (from left to right) the orbit of sub 10 in the *x*–*y* plane and its distance to the centre of the MW halo, as well as the evolution of its total mass and maximum circular velocity $v_{\rm max}$. As in previous plots, the DMO and Hydro simulations are represented by black and red colours, respectively. In the last two panels, a vertical line represents the end of reionization in the Hydro simulation.

features in quasar spectra suggest that reionization began as early as $z \sim 14$ and ended at $z \sim 6$ (Fan et al. 2006).

The majority of the low-mass subhaloes in our simulations are unable to form any stars due to reionization, thus staying dark. In Fig. 13, we show the evolutionary histories of five of such dark subhaloes, sub 149, 252, 347, 277, and 382. The trajectories show that they have been recently accreted on to the main halo. For each subhalo, the trajectory from the Hydro simulation is close to that

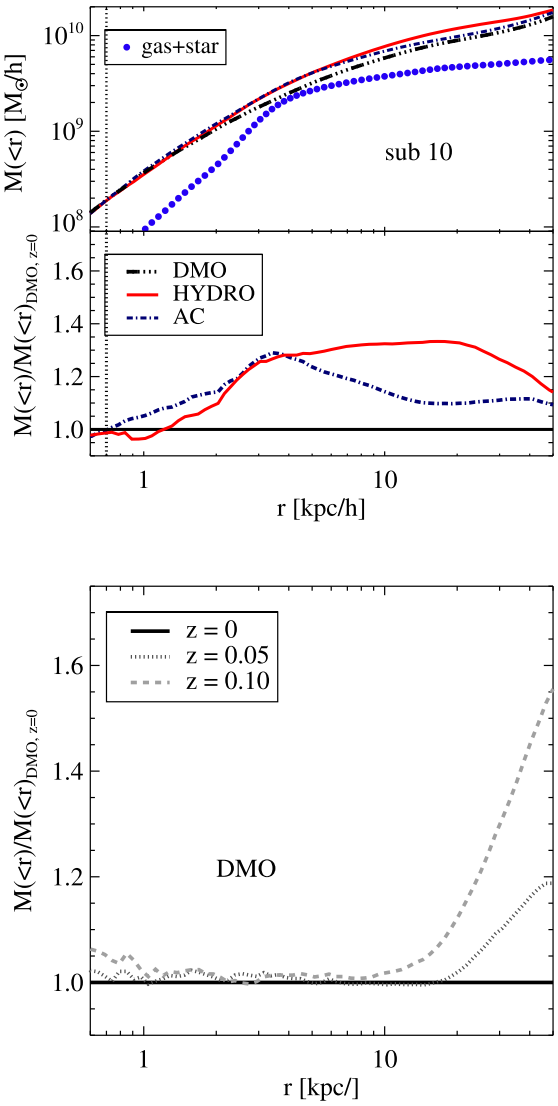

Figure 12. Top panel: comparison of the radially enclosed DM mass profiles of sub 10 from different simulations. The red solid, black triple dot–dashed, and blue dash–dotted curves represent the Hydro simulation, the DMO simulation, and CONTRA calculation, respectively, and the total enclosed baryonic mass (gas and stars) is also shown (blue filled circles). A factor of $\frac{\Omega_m-\Omega_b}{\Omega_m}$ is applied to the density profile from the DMO simulation. This plot shows that sub 10 retains more mass in the outer region in the Hydro simulation than its DMO counterpart. Bottom panel: the radially enclosed DM mass profiles of sub 10 in the DMO simulation at different evolution times. This subhalo has a pericentric passage at redshift $z = 0.10$ in both simulations. In the DMO simulation, this subhalo experienced substantial mass-loss in the outer region which explains the difference between the two mass profiles in the top panel beyond 10 kpc.

of the DMO simulation, albeit with some small deviations. This is expected since the gravitational potential of the central host is modified in the hydrodynamic simulation due to the presence of the stellar disc, and the gas ram pressure, which is absent in collisionless *N*-body simulations, introduces some additional offsets in orbital phase space.

The growth history of each subhalo shows remarkable differences between the DMO and Hydro simulations after $z = 6$. The subhalo mass from the Hydro simulation is consistently lower than that from the DMO simulation. It is clear that the gas content of the subhaloes declines rapidly after reionization, because the shallow gravitational potential of these objects both fails to retain the heated gas and to accrete new gas from the IGM.

A comparison of the growth histories between Figs 13 and 11 shows that only the more massive subhaloes are able to retain their gas after reionization, likely due to the fact that the densest gas regions in these objects can still reach the critical density needed for self-shielding from the ionizing UV background. These subhaloes also have a sufficiently deep gravitational potential to accrete new gas and sustain star formation. These results are consistent with those obtained by Oñorbe et al. (2015) for simulations of field dwarf galaxies, and demonstrate that reionization significantly suppresses the formation of low-mass galaxies.

4.1.3 The role of tidal disruption

The third group we consider consists of bright satellites (intermediate-mass subhaloes with 20 km s^{-1} < v_{max} < 35 km s^{-1}) similar to the dSph galaxies near the MW. We have already shown in Fig. 3 the effect of increased tidal disruption of subhaloes in the Hydro simulation, which resulted in a lower subhalo abundance in the inner region of the main halo. Below we will examine individual subhaloes and how they are shaped by tidal forces.

In Fig. 14, we map the distribution of the DM components of two satellites, sub 436 and 244, at $z = 0$, both in the Hydro and DMO simulations. For the Hydro simulation, we also examine the stellar distribution. The original members of each subhalo are identified at the redshift when their v_{max} reached the peak value. Overall, the trajectories of the matched subhaloes are similar in the Hydro and DMO simulations, but with some subtle differences. For example, the current positions of the two subhaloes in the DMO simulation lag slightly behind those in the Hydro simulation. This may be caused by the deeper potential well of the main halo from a more contracted DM density profile and the presence of the stellar disc, which accelerate the subhaloes close to the host to move at a slightly higher speed in the Hydro simulation than in the DMO one. However, the most striking feature visible in the figure is the presence of tidal debris and streams of both DM and stars. This is clear evidence of strong gravitational interactions and tidal truncation of these two satellites.

Fig. 15 shows the evolutionary paths and growth histories of four subhaloes (sub 220, 162, 244, 436) that are massive enough to retain gas to fuel star formation in a continuous manner after reionization. The typical stellar mass of these subhaloes falls in the range of 10^6–10^7 h^{-1} M$_\odot$ at $z = 0$, similar to that of the classical dSph galaxies in the Local Group (Boylan-Kolchin et al. 2012). These dwarfs have a total mass well above 10^9 h^{-1} M$_\odot$ before infall to the main host, and they can continue to accrete gas from the IGM after $z = 6$.

These subhaloes experienced strong gravitational interactions with their main host before the final plunges, as shown in their trajectories. These encounters tidally remove both baryons and DM, resulting in a steady reduction of the subhalo mass. The interactions also trigger episodes of starbursts, as shown in the growth curve of the stellar mass, and lead to distinct step-wise fluctuations in the velocity curve. The v_{max} curves experience stronger reductions in the Hydro simulation than in the DMO one. These are characteristic features of tidal forces during pericentre passages of the central galaxy. These findings are consistent with idealized simulations of tidal disruption of dwarf galaxies by Peñarrubia, Navarro & McConnachie (2008b) and Arraki et al. (2014).

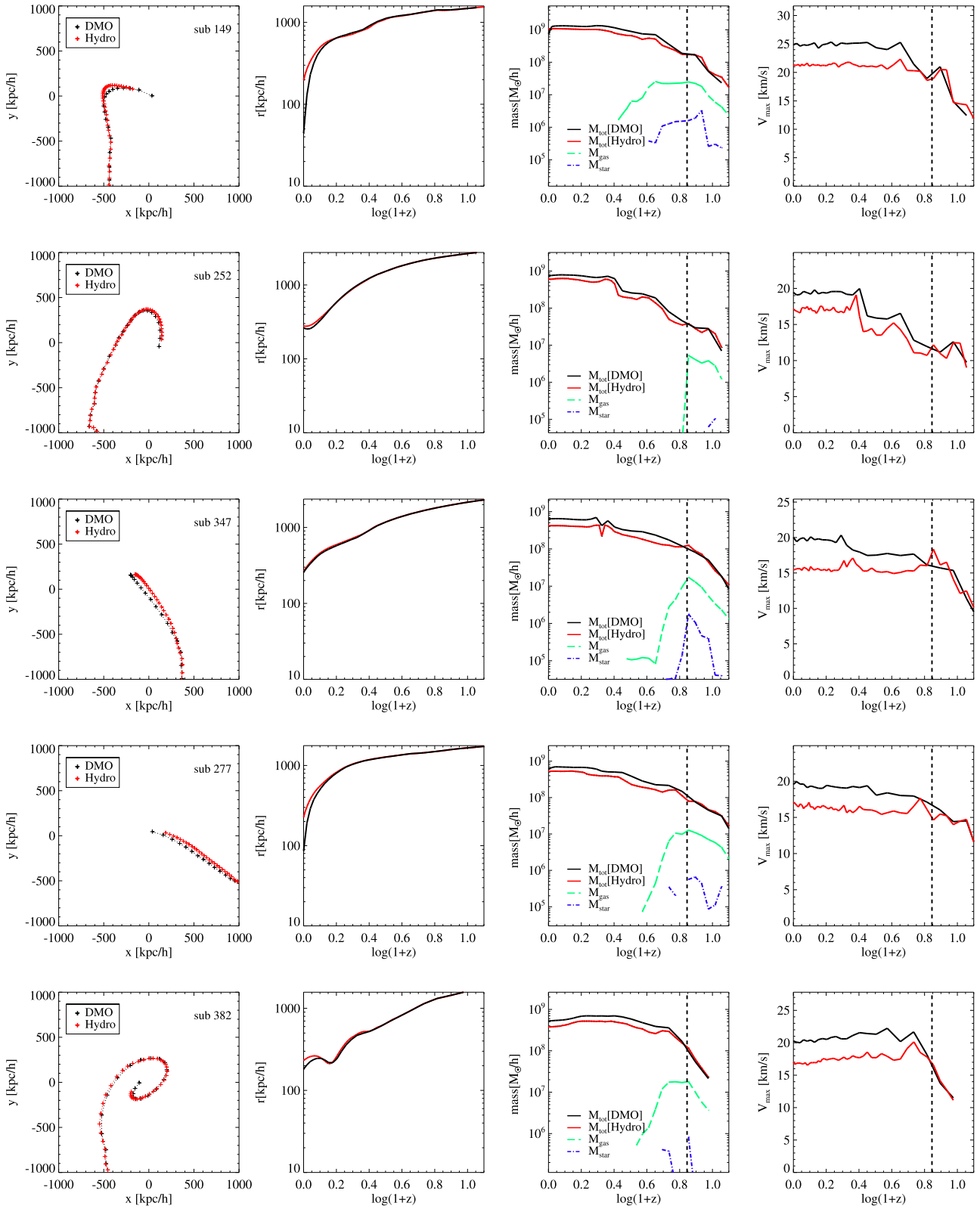

Figure 13. The evolution of five low-mass subhaloes ($v_{\rm max} < 20\,{\rm km\,s^{-1}}$) from the simulations (namely sub 149, 252, 347, 277, and 382) in terms of their orbits in the x–y planes and their distance to the centre of the MW halo at different redshifts (left two columns). Also shown are their growth histories in mass and circular velocity as a function of redshift (right two columns). As in previous plots, the DMO and Hydro simulations are represented by black and red colours, respectively. In the two columns on the right, the total, gas, and stellar masses are represented by solid, green dash–dotted, and blue dotted lines, respectively, and the vertical dashed line indicates the end of reionization at $z = 6$.

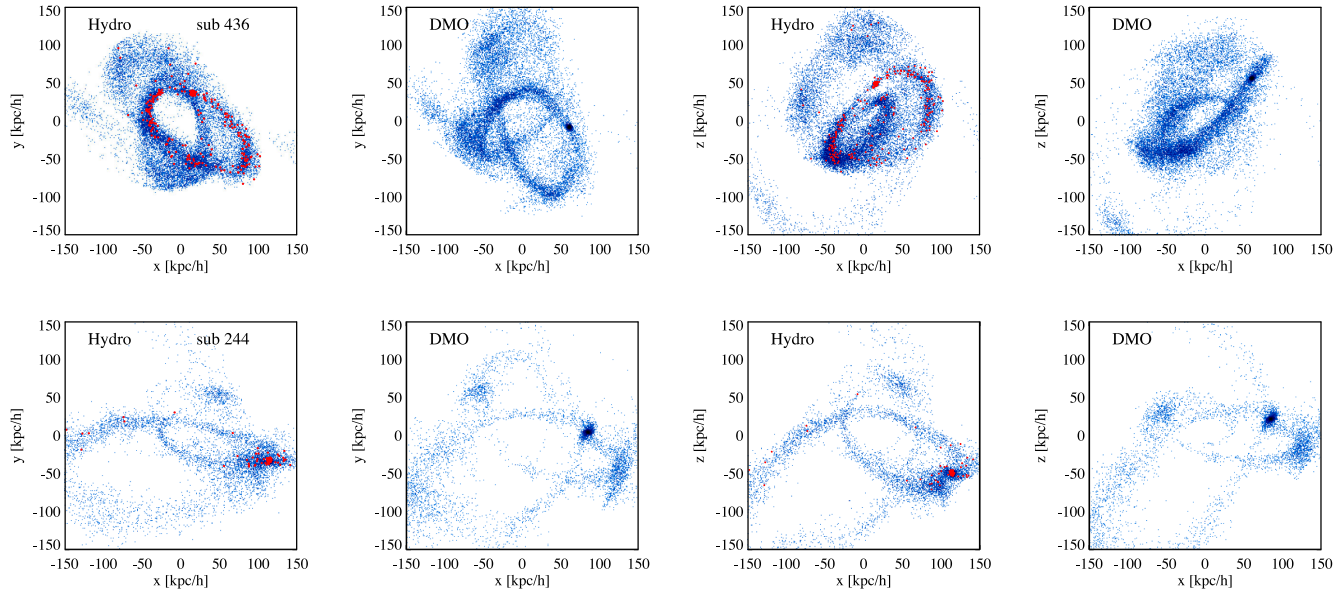

Figure 14. Projected maps of the DM distribution of two bright satellites (intermediate-mass subhaloes with 20 km s^{-1} < v_{max} < 35 km s^{-1}), namely sub 436 (top panels) and 244 (bottom panels), at $z = 0$ from both the Hydro and DMO simulations. The left two columns show projections in the x–y plane, while the right two columns show the projections in the x–z plane. The blue dots represent the DM particles, while red dots show stars in the Hydro simulation. The presence of both DM and stellar streams in these plots is a clear sign of tidal truncation.

In addition, the dwarf galaxies end up gas poor at $z = 0$ in the simulation, as shown in the evolution curve of the gas mass in Fig. 15. All four dwarfs have experienced an abrupt loss in gas mass during their first infall. Gas is loosely bound to the subhaloes compared to their stellar and DM components. However, tidal forces alone could not completely remove the gas. In principle, tidal torques may well funnel some gas into the centre of these dwarfs and compress it to form a dense component which is difficult to strip (Mayer et al. 2006). However, ram pressure, on the other hand, is able to efficiently remove the gas from these subhaloes when they pass through the hot halo gas of the central galaxy (Mayer et al. 2006; Wadepuhl & Springel 2011; Gatto et al. 2013; Arraki et al. 2014). Ram-pressure stripping can transform these dwarf galaxies into gas-poor systems, and it may also induce other effects. For example, it was suggested by Arraki et al. (2014) that sudden gas loss in a dwarf galaxy due to ram pressure could cause its DM to expand adiabatically and thus reduce v_{max}. However, this effect is small (<10 per cent in v_{max}) compared to the much larger reduction in v_{max} caused by tidal truncation.

The trends of total mass evolution of subhaloes in Fig. 15 show clear tidal disruption caused by the central galaxy. The signature of tidal disruption is also clearly seen in the sharp and distinct decrease of v_{max}. We show in Fig. 16 the evolution of three subhaloes with even shorter pericentric distances, comparable to the stellar disc size of ∼25 kpc of the central galaxy (Marinacci et al. 2014a). Not surprisingly, these subhaloes experience even more substantial reductions in both mass and v_{max} during their close encounters with the host galaxy. In particular, subhaloes 3309 and 745 show the largest reduction in v_{max} (∼50 per cent of their DMO values) since they have passed the galactic centre at much smaller distances (∼20 kpc) than the other subhaloes. The mass-loss in the stellar component is also higher for these three subhaloes than those in Fig. 15.

The enhanced tidal disruption rate in the Hydro simulation is likely a combination of several gravitational effects, such as halo shocking from a rapidly varying potential which induces tidal shocks when the objects are on highly eccentric orbits, and disc shocking when they are passing in the vicinity of the stellar disc. In comparison, tidal stripping of material is a gentler process that does not increase the kinetic energy within the subhalo, at least when strong resonances are not operating (D'Onghia et al. 2009, 2010b). To investigate the impact of tidal shocks on satellites, we follow the evolution of σ/v_{max}, a ratio between the DM velocity dispersion σ and the maximum circular velocity v_{max}, a proxy of energy. In Fig. 17, we show subhalo 244 as an example during its infall journey into the main galaxy. Indeed, the internal energy of the subhalo, as indicated by σ/v_{max}, increases sharply when it passes the pericentre of its trajectory, demonstrating heating from tidal shocks during the close encounter. We have confirmed that the peaks of σ/v_{max} are caused by the increase of σ when the subhalo passes pericentre. We note, however, that only 64 snapshots were stored for the entire simulation, with the consequence that the time sampling is not ideal for probing the subhalo trajectory at the time resolution required to clearly disentangle tidal from disc shocking or halo shocking. The discrete time sampling may also likely overestimate the 'minimum distance' plotted in these figures while the true 'minimum distance' is attained between two snapshots.

4.1.4 The origin and evolution of bright and dark subhaloes

To understand the origin of 'bright' (with stars) and 'dark' (without stars) subhaloes in the mass range of 10^8–10^9 h^{-1} M$_\odot$, we track their assembly histories in our simulations. In Fig. 18, we show the distance of each subhalo to the central galaxy during its infall. Interestingly, 'bright' and 'dark' subhaloes have different accretion paths. On average, the bright satellites are accreted into the host at an earlier redshift than the majority of the dark subhaloes, and they typically undergo multiple passages through the main halo. Moreover, we follow the evolution of their v_{max} value and find that bright and dark subhaloes have different trends as well, as shown in Fig. 19. The dark subhaloes experience a sharp decline in v_{max} (or mass) shortly after the end of reionization, while the bright

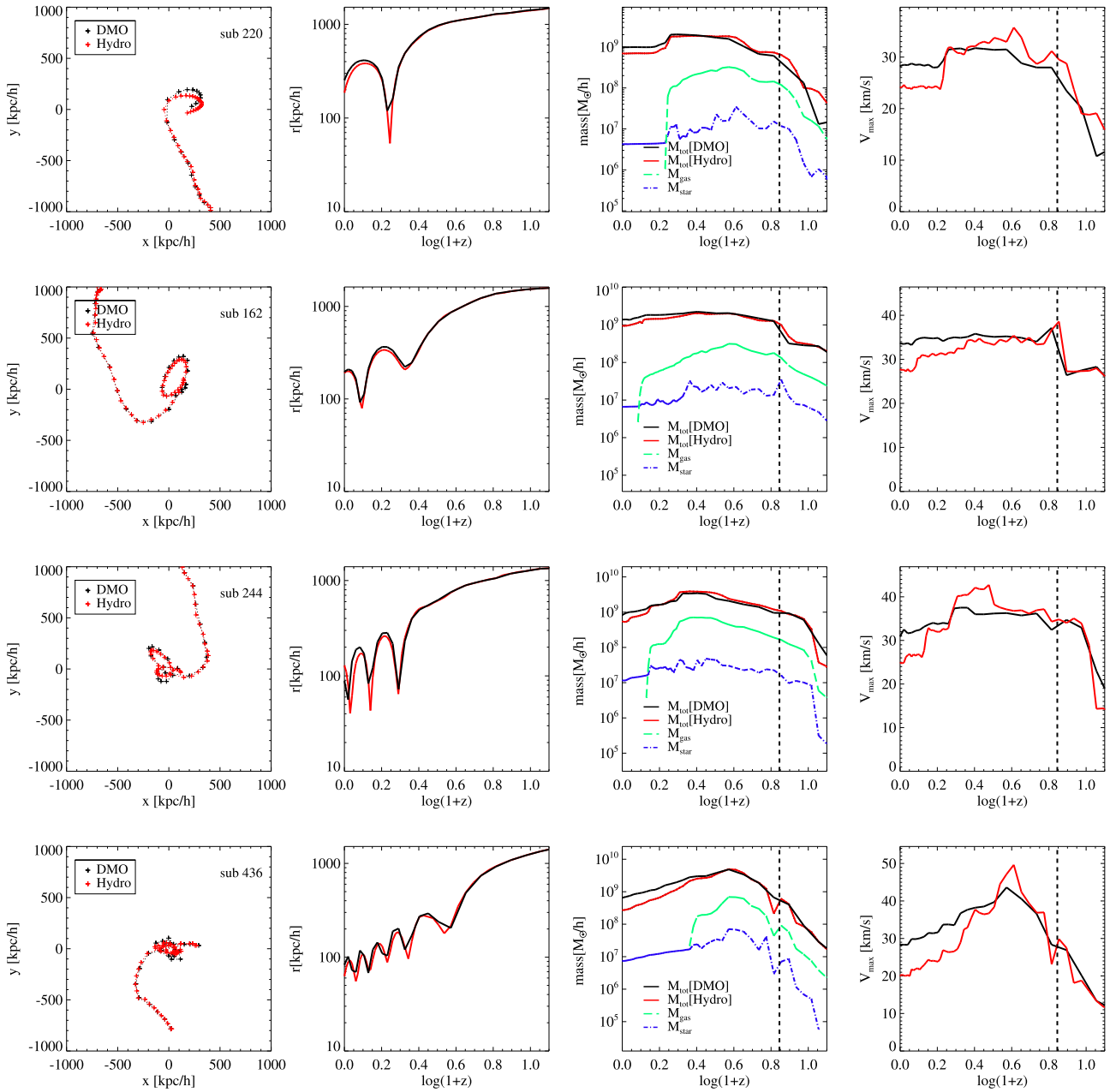

Figure 15. The evolution of four bright satellites (intermediate-mass subhaloes with 20 km s^{-1} < v_{max} < 35 km s^{-1}) from the simulations (namely sub 220, 162, 244, and 436) in terms of their orbits in the *x*–*y* plane and their distance to the centre of the MW halo at different redshifts (left two columns). Their growth histories in mass and circular velocity as a function of redshift are also shown (right two columns). As in previous plots, the DMO and Hydro simulations are represented by black and red colours, respectively. In the two columns on the right, the total, gas, and stellar masses are represented by solid, green dash–dotted, and blue dotted lines, respectively, while the vertical dashed line indicates the end of reionization at $z = 6$.

satellites do not show such an immediate and dramatic suppression by reionization. In fact, most of them are able to retain the existing gas and replenish some of it long after $z = 6$, thus boosting their mass growth. In both cases, there is a reduction of v_{max} by ∼17 per cent on average at $z = 0$ in the Hydro simulation compared to the DMO one, highlighting the effects of baryonic processes on mass reduction discussed in the previous sections.

As demonstrated in Fig. 19, reionization plays an important role in the formation of bright and dark satellites. The impact of reionization on these subhaloes is mainly to suppress fresh gas accretion from the IGM, as evidenced by a dip in the curve of the dark subhaloes around $\log(1 + z) \sim 0.65$ ($z \sim 3.5$). However, a number of the bright satellites in our simulation gain substantial mass even after $z \sim 3$ (see also Fig. 13). Ricotti (2009) considered a scenario in which the low-mass haloes (v_{max} < 20 km s^{-1}) in the outer region of the MW are able to accrete low-density IGM gas after $z = 3$ and form stars, once the mean temperature of the low-density IGM starts to decrease due to Hubble expansion, similar to what we find here.

Our simulations show that bright satellites have a different origin and evolutionary path from the dark ones. At early times, the bright satellites survive better than dark subhaloes from reionization, and they are able to retain gas and form stars afterwards. Moreover, they have an earlier infall time into the main galaxy than the dark

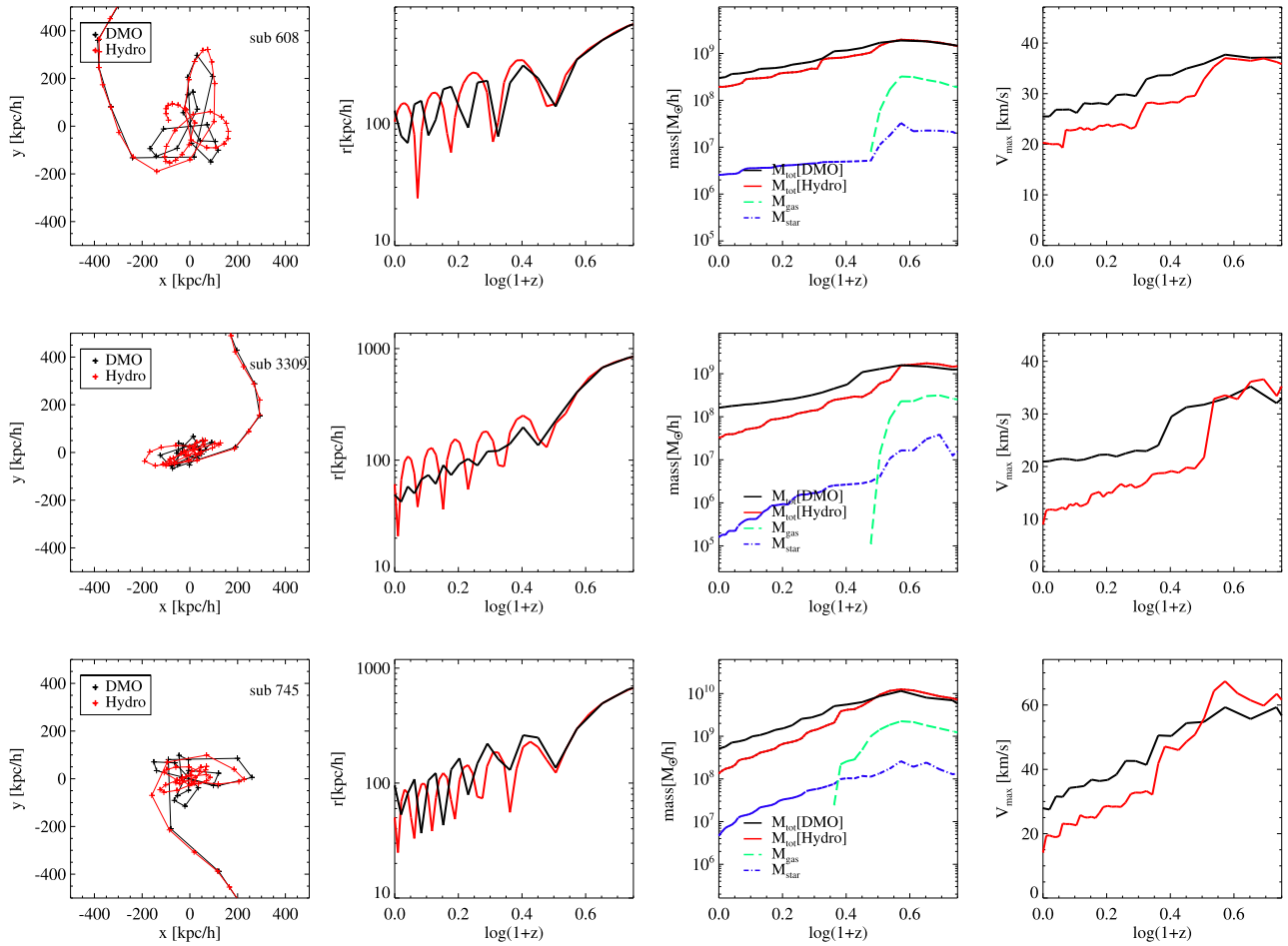

Figure 16. Same as Fig. 15, but for three subhaloes (namely sub 608, 3309, and 745) with closest encounters with the central galaxy at distances comparable to the stellar disc size of ∼25 kpc. As in previous plots, their orbits in the x–y plane and their distance to the centre of the MW halo at different redshifts are shown in the left two columns, and their growth histories in mass and circular velocity as a function of redshift are shown in the right two columns. The DMO and Hydro simulations are indicated by black and red colours; the total, gas, and stellar masses are represented by solid, green dash–dotted, and blue dotted lines, respectively. Note that the redshift range $\log(1+z)$ is slightly narrowed compared to Fig. 15 to highlight the temporal evolution of $v_{\rm max}$, distance, and mass.

ones, as also reported by other work (Sawala et al. 2016). Our results suggest that bright satellites may be biased tracers of the total subhalo population, as implied by observations of faint dwarfs of the Local Group (Weisz et al. 2015).

5 DISCUSSION

Thanks to significant progress in numerical modelling of galaxy formation and evolution, recent hydrodynamic simulations are becoming increasingly successful and are now able to reproduce many of the observed properties of galaxies in a more self-consistent manner. However, the complexity of the physical processes and the numerical methods inevitably entail uncertainties in the modelling. In what follows, we will compare our simulations with previous work and discuss the limitations of our model.

5.1 DM 'cores'

First of all, it is useful to compare the impact of baryons on the distribution of DM in an MW-sized halo found in our study with other works. The enhanced DM concentration in the inner region of the main halo seen in our simulation is consistent with adiabatic contraction. Moreover, we do not find cored DM distributions on dwarf galaxy scales in our simulation. Recently, both Macciò et al. (2012) and Mollitor et al. (2015) have reported flattened DM distributions within 5 kpc from the galactic centre in their hydrodynamic simulations of haloes with similar mass. This difference cannot be attributed to insufficient numerical resolution as our mass resolution and gravitational softening length, which is finer than in Macciò et al. (2012), should give reliable results on kpc scales (Power et al. 2003; Springel et al. 2008). It is also unlikely to arise from differences in the hydrodynamics or gravity solvers, because grid-based codes such as RAMSES used in Mollitor et al. (2015) do not have the problem of intrinsic noise in smoothed particle hydrodynamics (SPH) methods (Bauer & Springel 2012; Zhu, Hernquist & Li 2015) and use independent and different numerical methods than employed in Macciò et al. (2012). The most plausible cause for the difference lies in the feedback models. Here all three simulations have used a similarly large fraction of SN energy to drive outflows. However, our outflow model is less bursty than those of Macciò et al. (2012) and Mollitor et al. (2015), and this has been suggested as an important factor for making cores. We note however that Garrison-Kimmel et al. (2013) argued that repeated blowout of gas

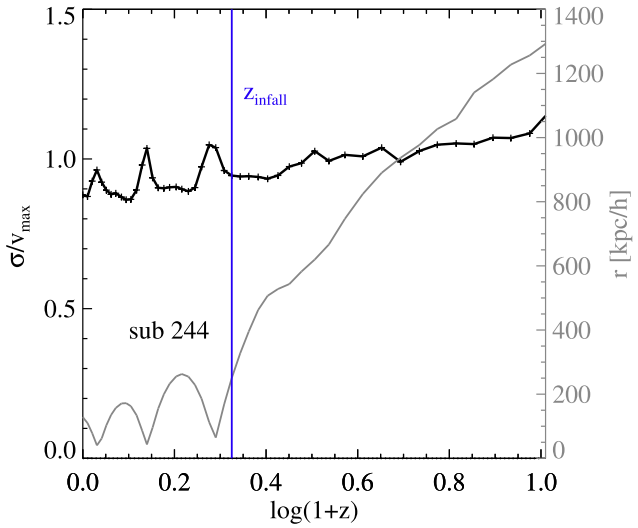

Figure 17. Effect of tidal shocks on the evolution of subhalo 244. The black solid curves represent the evolution of $\sigma/v_{\rm max}$, while the grey solid line represents the distance of sub 244 to the centre of the MW halo at different redshifts (in comoving units). Each peak of $\sigma/v_{\rm max}$ corresponds to a sharp increase of random kinetic energy due to tidal shock heating when the satellite passes through the pericentre. A blue vertical line indicates the infall time of this object at $z = 1.1$, when it has first become a subhalo of the central host.

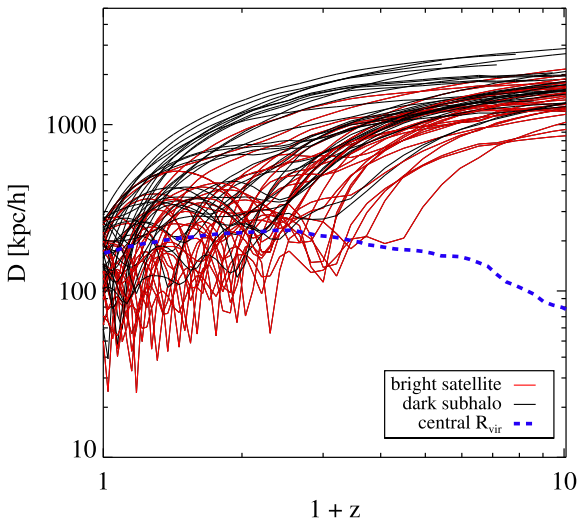

Figure 18. The distances (in comoving units) to the central galaxy of all subhaloes in the mass range of 10^8–10^9 $M_\odot$ at different times during their infall to the host, taken from the Hydro simulation. The red and black solid curves represent 'bright' (with stars) and 'dark' (without stars) subhaloes, respectively, while the blue dashed curve indicates the virial radius of the main galaxy at different redshift.

is not necessarily more effective than a single blowout in reducing central DM densities.

The outflow model used here is phenomenological and ties the wind launching velocity directly to the properties of subhaloes. Once flagged as a wind, outflowing particles are temporally decoupled from hydrodynamics to prevent a disruption of the sub-resolution ISM phase. Thus, the small-scale creation of the wind in a star-forming region and its interaction with the ISM are not followed in detail. Dalla Vecchia & Schaye (2008) have argued that such a decoupled wind is less efficient than a coupled wind in

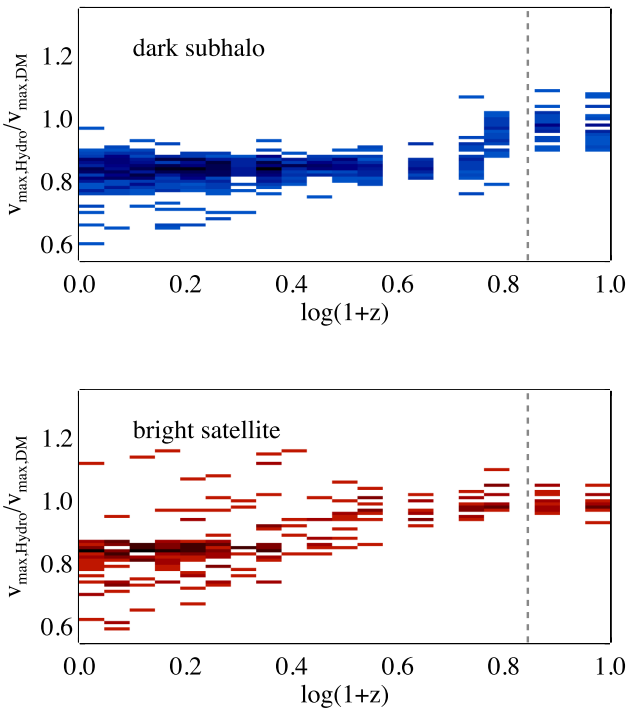

Figure 19. Evolution of the maximum circular velocity of both dark (top panel) and bright (bottom panel) subhaloes in the mass range of 10^8–10^9 $M_\odot$. These subhaloes are identified in the Hydro simulation. In order to compare with the DMO simulation and to identify the effects of baryons, the ratio $v_{\rm max,\,Hydro}/v_{\rm max,\,DM}$ of matched subhaloes in both simulations is used. The vertical dashed line represents the end of reionization at redshift $z = 6$. The redshift bin size is 0.05 due to the limited number of output snapshots available for the simulations.

driving strong turbulent motions on the scale of dwarf galaxies. A decoupled wind scheme could thus in principle miss some of the physical processes needed to generate DM cores, provided random bulk motions of gas are indeed able to produce a strongly fluctuating gravitational potential, as argued by Mashchenko, Couchman & Wadsley (2006) and Pontzen & Governato (2012, 2014). However, Sawala et al. (2014) reported that their simulated galaxies do not contain cores, even though they use a coupled wind model. This indicates that the decoupling feature of the wind model we used is not responsible for the absence of DM cores in our run. It thus remains interesting to see on what time-scales the gravitational potential needs to fluctuate to generate DM cores. It is also possible that the delayed cooling mechanism used by Macciò et al. (2012) and Mollitor et al. (2015) overestimates the effect of bursty SN explosions (Agertz et al. 2013).

Despite this difference between our simulation and others that predict DM cores, our results regarding the 'dark' subhaloes and the least luminous dwarfs should not be affected by the wind model, because these objects have the lowest star formation activities and hence an efficient removal of DM is energetically difficult (e.g. Governato et al. 2012; Garrison-Kimmel et al. 2013; Di Cintio et al. 2014; Madau et al. 2014; Oñorbe et al. 2015). Indeed, Di Cintio et al. (2014) predicted that the most cored density distribution is likely to be found in large haloes with $v_{\rm max} = 50$ km s^{-1}, and that DM profiles remain cuspy for dwarf galaxies with the least massive stellar population, in line with some recent hydrodynamic simulations of field dwarf galaxies (Madau et al. 2014; Oñorbe et al. 2015). The reduction on $v_{\rm max}$ at the low-mass end

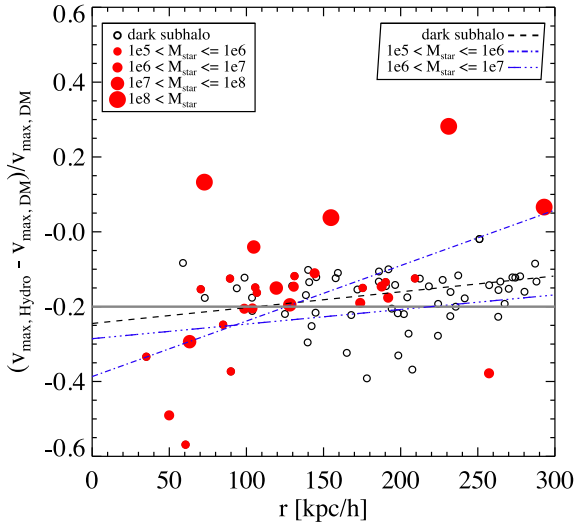

Figure 20. The radial distribution of the reduction of $v_{\rm max}$ ($\Delta v_{\rm max} = (v_{\rm max,\,Hydro} - v_{\rm max,\,DM})/v_{\rm max,\,DM}$) of matched subhaloes between Hydro and DMO simulations. The open black circles represent the dark subhaloes that contain no stars, while each of the filled red circles represents individual bright satellite with its size proportional to the subhalo mass. The black dashed and the blue lines are simple linear fittings to the dark subhaloes, and bright subhaloes in the mass ranges 10^5 M$_\odot$ $< M_{\rm star} < 10^6$ M$_\odot$ and 10^6 M$_\odot$ $< M_{\rm star} < 10^7$ M$_\odot$, respectively, while the grey horizontal line provides a visual guide of no correlation between $\Delta v_{\rm max}$ and galactic distance r. Overall, there is no clear radial dependence of $\Delta v_{\rm max}$ of the subhaloes in our simulations. Note the weak $\Delta v_{\rm max}$–r relation of subhaloes with 10^5 M$_\odot$ $< M_{\rm star} < 10^6$ M$_\odot$ is due to two outliers at $r = 50\ h^{-1}$ kpc. Once these two outliers are removed from the sample, the resulted radial dependence is as weak as the 'dark' subhaloes and those with 10^6 M$_\odot$ $< M_{\rm star} < 10^7$ M$_\odot$.

($v_{\rm max} < 20$ km s^{-1}, mostly 'dark') of the cumulative subhalo mass function in our simulation is in good agreement both with other SPH (Zolotov et al. 2012; Sawala et al. 2014) and AMR (Mollitor et al. 2015) simulations, and we believe that reionization is the primary culprit for the suppressed gas accretion rate from the IGM and the reduced number density of low-mass subhaloes.

5.2 Tidal disruption

It was argued by Tollerud et al. (2014) that tidal forces play a marginal role in resolving the 'too big to fail' problem as there is a lack of a strong radial dependence in the r–$v_{\rm max}$ relation for the M31 satellite galaxies. However, we find no strong radial dependence in the reduction of $v_{\rm max}$ in terms of $(v_{\rm max,\,Hydro} - v_{\rm max,\,DMO})/v_{\rm max,\,DMO}$ in the Hydro simulation, as shown in Fig. 20. Overall, the distribution of $(v_{\rm max,\,Hydro} - v_{\rm max,\,DMO})/v_{\rm max,\,DMO}$ is rather flat, close to -0.2, as a function of distance r. In this figure, we further divide the subhaloes into several subgroups according to their stellar mass and fit the results with simple linear functions. Only the subhalo sample with 10^5 M$_\odot$ $< M_{\rm star} < 10^6$ M$_\odot$ shows a clear radial dependence. However, this strong radial trend is dominated by two subhaloes. If we remove the two outliers around $50\ h^{-1}$ kpc, the radial trend disappears accordingly. For subhaloes with 10^6 M$_\odot$ $< M_{\rm star} < 10^7$ M$_\odot$, which is in the same mass range as the dSphs in Tollerud et al. (2014), there is no clear radial dependence for the reduction of $v_{\rm max}$. Hence, we conclude that a lack of a strong radial dependence cannot refute the role of tidal disruption.

Tollerud et al. (2014) attributed the reduction of the number of subhaloes to SN feedback. However, we find that this plays a minor role in our simulation, especially for the subhaloes with an intermediate $v_{\rm max}$ (see Fig. 14), in which the (maximum) circular velocity is always larger in the Hydro case than in the DMO one before those objects are accreted into the central galaxy where stronger tidal disruption in the Hydro simulation comes into play. In our simulations, the tension between ΛCDM and observations of dwarf galaxies leading to the so-called 'too big to fail' problem is largely alleviated by stronger tidal disruption, caused by an enhanced DM concentration and the stellar disc of the central galaxy (see also Romano-Díaz et al. 2010). The problem is further mitigated by the fact that these subhaloes are accreted by the host at a much earlier time than the average 'dark' subhaloes as shown in Fig. 18. Thus, they have experienced a more extended tidal influence from their host galaxy compared to the average subhalo. On the other hand, if the host halo in our simulation is slightly less massive, similar to the halo masses used by other groups (e.g. Guedes et al. 2011; Sawala et al. 2014), one may not have a 'too big to fail' problem at all to begin with (Wang et al. 2012). However, it is unclear how tidal disruption or similar environmental effects would work for the recently reported 'too big to fail' problem of field dwarf galaxies (Garrison-Kimmel et al. 2014b; Klypin et al. 2015; Papastergis et al. 2015).

5.3 Mass reduction

A number of previous works have examined the effects of baryons on haloes in different mass ranges (e.g. Sawala et al. 2013; Schaller et al. 2015). In order to compare with these studies, we show in Fig. 21 the reduction of mass and $v_{\rm max}$ from different simulations. The top panel compares the total mass reduction in the haloes/subhaloes as a function of subhalo mass from our simulations with the fitting relations from Sawala et al. (2013, GIMIC simulation) and Schaller et al. (2015, EAGLE simulation), as well as all subhaloes from the matched catalogue between the Illustris and Illustris-Dark simulations (Nelson et al. 2015).[3] To allow for a comparison with our results, we extrapolated the fitting relations of Sawala et al. (2013) and Schaller et al. (2015) down to 10^8 M$_\odot$. Given the form of these relations, this is equivalent to using a constant value of 0.65 and 0.73, respectively, for subhaloes less massive than $\sim 10^8$ M$_\odot$. Under this assumption, the plot shows that all studies are in good agreement for the mass reduction of the central MW-sized galaxy, as well as the low-mass end ($< 5 \times 10^9$ M$_\odot$) where most of the dark subhaloes and bright satellites in our simulations are located. There is substantial scatter in $M_{\rm 200,\,Hydro}/M_{\rm 200,\,DMO}$, which is both evident in the data points and the error bars of the Illustris results. We show a moving average of 200 data points with a thick solid black curve to highlight the overall trends in the low-mass range covered by the high-resolution simulation used in this study.

However, significant differences are present in the mass range between 5×10^9 and 10^{12} M$_\odot$. The mass ratio given by Sawala et al. (2013) or Schaller et al. (2015) is evidently lower than ours. Although we suffer from small-number statistics in our simulation, the mass excess in the Hydro simulation appears to be a real signal as also shown by a much larger galaxy sample drawn from the Illustris matched subhaloes. Considering that the universal baryonic mass fraction is ∼16 per cent, galaxies in Sawala et al. (2013) or

[3] Raw data from each simulation are available from http://www.illustris-project.org/data/.

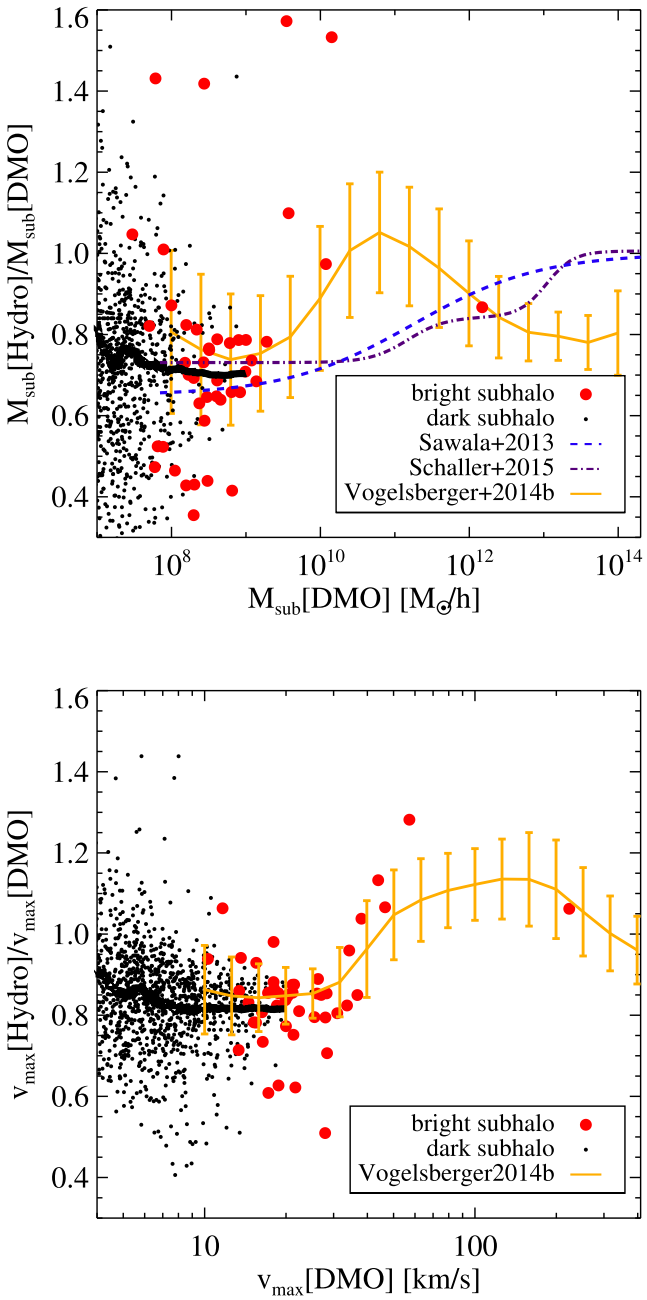

Figure 21. A comparison of our work with previous studies of the reduction of mass and $v_{\rm max}$. Top panel: ratio of $M_{\rm sub}$[Hydro]/$M_{\rm sub}$[DMO] as a function of subhalo mass $M_{\rm sub}$[DMO] from our simulations and fitting relations from Sawala et al. (2013), Schaller et al. (2015), and Vogelsberger et al. (2014a). The filled symbols indicate our simulation data (red for bright satellites, black for dark subhaloes), while the relations from Sawala et al. (2013, GIMIC simulation) and Schaller et al. (2015, EAGLE simulation) are shown as long-dashed and dash–dotted lines, respectively. We include all the matched subhaloes between the Illustris full physics run and Illustris-Dark without further separating them into subsamples as in Vogelsberger et al. (2014a, yellow line). Scatter from the fitting relations, shown as 1σ error bars, is computed within each mass bin. Bottom panel: ratio of $v_{\rm max}$[Hydro]/$v_{\rm max}$[DMO] as a function of $v_{\rm max}$[DMO]. The scatter of this relation, as indicated by 1σ error bars, is smaller than the top panel for Illustris. In both panels, a moving average of 200 data points is shown (black thick solid curve) to highlight the overall trend in the low-mass range.

Schaller et al. (2015) actually have less mass in the DM component in their hydrodynamic simulations. This led them to conclude that SN feedback, which is strongly operating in this mass range, has also removed some DM, thus producing lighter haloes. However, we do not see DM mass reduction in this mass range in our simulation. As we have found in our earlier discussions on sub 10 ($v_{\rm max}$ = 73 km s^{-1}), we actually observe an increased DM mass in this regime due to adiabatic contraction.

We note that the mass values returned by halo finders do have some uncertainties, which is evident in the large scatter of the raw data in the upper panel of Fig. 21, while $v_{\rm max}$ is not as severely affected (e.g. Behroozi et al. 2015). In the lower panel of Fig. 21, we compare the ratio of $v_{\rm max}$[Hydro]/$v_{\rm max}$[DMO] from our simulations with that of the Illustris simulations. Both works show good agreement over the common $v_{\rm max}$ range, with subhaloes above $v_{\rm max}$ $\sim$ 35 km s^{-1} ($M_{\rm sub} > 5 \times 10^9$ M$_\odot$) having higher $v_{\rm max}$ in the hydrodynamic simulation than in their DMO counterpart. Similar to the top panel, we show a moving average of 200 data points at the low-$v_{\rm max}$ end with a thick solid black curve to highlight the overall behaviour, which is consistent with the Illustris relation.

Since our simulations employ the same code and essentially the same physical models as the Illustris simulations, the differences between our study and previous ones by Sawala et al. (2013) and Schaller et al. (2015) may owe to different implementation of feedback processes or different hydrodynamical methods used in these works. These comparisons thus highlight the need for comprehensive and systematic investigations similar to the Aquila Comparison Project, which is beyond the scope of this paper, but we plan to pursue it in future work.

5.4 Implications for DM detections

N-body simulations are routinely used to model direct/indirect signals from Galactic DM structures. However, all the recent studies agree that baryons have significant impacts on DM distributions. The interplay between baryonic and DM distributions has a direct impact on current attempts to indirectly measure DM in the MW as well as in other galaxies. Traditionally, DM substructures are thought to be responsible for the observed radio flux-ratio anomaly in gravitational lensing (e.g. Mao & Schneider 1998). Recent studies by Xu et al. (2010, 2015) based on the *N*-body simulations by Springel et al. (2008) and Gao et al. (2012) concluded that DM substructures alone cannot be the whole reason for radio flux-ratio anomalies. Xu et al. (2015) suggested that a substantial improvement over the existing modelling of strong lensing would be to consider substructures in baryonic simulations that take the impact of baryonic processes on DM into account. Similarly, accurate predictions of the DM annihilation rate (The Fermi-LAT Collaboration 2014) sensitively depend on the DM distribution in the dwarf galaxies. The uncertainties in the DM distributions enter in factors describing the clumping of the DM density (proportional to the density squared) along the line of sight (see Geringer-Sameth, Koushiappas & Walker 2015). For example, Gómez-Vargas et al. (2013) have shown that the cross-section estimated from γ-ray photons from the galactic centre can be affected by adiabatic contraction of DM by more than an order of magnitude. So far, these studies are based on inferences from high-resolution *N*-body simulations. Hydrodynamical simulations change this picture and offer a more accurate and self-consistent physical modelling for analysing direct and indirect detection experiments.

6 CONCLUSIONS

The availability of hydrodynamical simulations allows us to reassess some of the well-known potential issues of ΛCDM that have been identified with pure *N*-body simulations. In particular, hydrodynamical simulations are able to self-consistently model the impact of baryonic processes on the DM distribution, a point which has previously often been ignored in galaxy formation studies based on DM-only simulations.

In this work, we analyse a high-resolution cosmological hydrodynamic simulation on a moving mesh and compare it to its DM-only counterpart in order to study the DM distribution in an MW-like galaxy and its subhaloes. This simulation uses essentially the same physical model employed in the Illustris simulation, and hence is consistent with a globally successful model for explaining the observed galaxy population. Moreover, the properties of the simulated galaxy are well converged with resolution, making our results numerically robust. Here we summarize our main findings.

(i) We identify three physical processes induced by baryons that shape the overall distribution of DM in the main halo and its subhaloes depending on mass: (1) adiabatic contraction due to gas cooling and condensation increases the DM concentration in the inner region of the main halo and in massive subhaloes with $v_{\rm max} > 35\,{\rm km\,s^{-1}}$ ($M_{\rm sub} > 4 \times 10^9\ h^{-1}\,{\rm M}_\odot$), making them more spherical in the inner regions; (2) reionization plays a critical role in the formation and evolution of low-mass haloes with $v_{\rm max} < 20\,{\rm km\,s^{-1}}$ ($M_{\rm sub} < 10^9\ h^{-1}\,{\rm M}_\odot$) by removing the gas from the halo and suppressing new gas accretion from the IGM, making them 'dark' with little or no star formation; (3) strong tidal forces in the Hydro simulation effectively remove the stellar and DM components of intermediate-mass subhaloes in the range of $v_{\rm max} \sim 20$–$35\,{\rm km\,s^{-1}}$ during their infall to the main galaxy, leaving behind tidal debris and streams of DM and stars.

(ii) As a result of these major effects from baryons, the total number of subhaloes in an MW-like galaxy and their total mass are significantly reduced in the hydrodynamic simulation compared to the DM-only one. Our results are in good agreement with observations of dwarf satellites in the MW galaxy, suggesting a viable solution to long-standing problems such as the 'missing satellites' and 'too big to fail' issues that arose from pure *N*-body simulations.

(iii) The ranking of subhaloes based on either their peak mass or their present-day mass is modified in the Hydro simulation compared with the DMO run. A large fraction of subhaloes with a peak mass below $10^9\,h^{-1}\,{\rm M}_\odot$ are found to host no stars. These findings suggest that the assumption of a monotonic relation between stellar mass and peak mass as commonly used in abundance matching is not strictly valid, and that effects of baryonic processes should be included in this modelling as well.

Interestingly, our high-resolution hydrodynamic simulation does not produce cored DM distributions as observationally suggested in some low surface brightness galaxies, and unlike some other recent simulation models with very bursty feedback modes. More sophisticated hydrodynamic simulations are needed to further study this puzzling problem, and to improve the realism of the inclusion of feedback processes to determine whether they can indeed provide a solution to small-scale tensions identified in the ΛCDM cosmogony.

ACKNOWLEDGEMENTS

We thank Steinn Sigurdsson, Priyamvada Natarajan, Annalisa Pillepich, Arthur Kosowsky, Eddie Chua, and Dylan Nelson for their suggestions and helpful discussions. We also thank an anonymous referee for valuable comments that have helped improve the manuscript. YL acknowledges support from NSF grants AST-0965694, AST-1009867, and AST-1412719. LH acknowledges support from NSF grant AST-1312095 and NASA grant NNX12AC67G. VS acknowledges support by the DFG Research Centre SFB-881 'The Milky Way System' through project A1, by the European Research Council under ERC-StG grant EXAGAL-308037, and by the Klaus Tschira Foundation. We acknowledge the Institute For CyberScience at the Pennsylvania State University for providing computational resources and services that have contributed to the research results reported in this paper. The Institute for Gravitation and the Cosmos is supported by the Eberly College of Science and the Office of the Senior Vice President for Research at the Pennsylvania State University.

REFERENCES

Addison G. E., Hinshaw G., Halpern M., 2013, MNRAS, 436, 1674
Agertz O. et al., 2007, MNRAS, 380, 963
Agertz O., Teyssier R., Moore B., 2011, MNRAS, 410, 1391
Agertz O., Kravtsov A. V., Leitner S. N., Gnedin N. Y., 2013, ApJ, 770, 25
Allen S. W., Evrard A. E., Mantz A. B., 2011, ARA&A, 49, 409
Amorisco N. C., Evans N. W., 2012, MNRAS, 419, 184
Arraki K. S., Klypin A., More S., Trujillo-Gomez S., 2014, MNRAS, 438, 1466
Aumer M., White S. D. M., Naab T., Scannapieco C., 2013, MNRAS, 434, 3142
Barnes J. E., Hernquist L. E., 1991, ApJ, 370, L65
Barnes J. E., Hernquist L., 1996, ApJ, 471, 115
Barnes J., White S. D. M., 1984, MNRAS, 211, 753
Bauer A., Springel V., 2012, MNRAS, 423, 2558
Behroozi P. et al., 2015, MNRAS, 454, 3020
Blumenthal G. R., Faber S. M., Flores R., Primack J. R., 1986, ApJ, 301, 27
Bosch F. C. v. d., Jiang F., Hearin A., Campbell D., Watson D., Padmanabhan N., 2014, MNRAS, 445, 1713
Boylan-Kolchin M., Bullock J. S., Kaplinghat M., 2011, MNRAS, 415, L40
Boylan-Kolchin M., Bullock J. S., Kaplinghat M., 2012, MNRAS, 422, 1203
Brooks A. M., Zolotov A., 2014, ApJ, 786, 87
Brooks A. M., Kuhlen M., Zolotov A., Hooper D., 2013, ApJ, 765, 22
Bryan S. E., Kay S. T., Duffy A. R., Schaye J., Dalla Vecchia C., Booth C. M., 2013, MNRAS, 429, 3316
Clowe D., Bradač M., Gonzalez A. H., Markevitch M., Randall S. W., Jones C., Zaritsky D., 2006, ApJ, 648, L109
Conselice C. J., 2014, ARA&A, 52, 291
Correa C. A., Wyithe J. S. B., Schaye J., Duffy A. R., 2015, MNRAS, 450, 1514
D'Onghia E., Besla G., Cox T. J., Hernquist L., 2009, Nature, 460, 605
D'Onghia E., Springel V., Hernquist L., Keres D., 2010a, ApJ, 709, 1138
D'Onghia E., Vogelsberger M., Faucher-Giguere C.-A., Hernquist L., 2010b, ApJ, 725, 353
Dalla Vecchia C., Schaye J., 2008, MNRAS, 387, 1431
Davé R., Spergel D. N., Steinhardt P. J., Wandelt B. D., 2001, ApJ, 547, 574
de Blok W. J. G., 2010, Adv. Astron., 2010, 5
Di Cintio A., Brook C. B., Dutton A. A., Macciò A. V., Stinson G. S., Knebe A., 2014, MNRAS, 441, 2986
Di Matteo T., Springel V., Hernquist L., 2005, Nature, 433, 604
Elbert O. D., Bullock J. S., Garrison-Kimmel S., Rocha M., Oñorbe J., Peter A. H. G., 2015, MNRAS, 453, 29
Evans N. W., An J., Walker M. G., 2009, MNRAS, 393, L50
Fan X. et al., 2006, AJ, 132, 117
Faucher-Giguère C.-A., Lidz A., Zaldarriaga M., Hernquist L., 2009, ApJ, 703, 1416
Frenk C. S., White S. D. M., 2012, Ann. Phys., 524, 507
Frieman J. A., Turner M. S., Huterer D., 2008, ARA&A, 46, 385

Gao L., Navarro J. F., Frenk C. S., Jenkins A., Springel V., White S. D. M., 2012, MNRAS, 425, 2169
Garrison-Kimmel S., Rocha M., Boylan-Kolchin M., Bullock J. S., Lally J., 2013, MNRAS, 433, 3539
Garrison-Kimmel S., Boylan-Kolchin M., Bullock J. S., Lee K., 2014a, MNRAS, 438, 2578
Garrison-Kimmel S., Boylan-Kolchin M., Bullock J. S., Kirby E. N., 2014b, MNRAS, 444, 222
Gatto A., Fraternali F., Read J. I., Marinacci F., Lux H., Walch S., 2013, MNRAS, 433, 2749
Genel S. et al., 2014, MNRAS, 445, 175
Geringer-Sameth A., Koushiappas S. M., Walker M. G., 2015, Phys. Rev. D, 91, 083535
Gilmore G., Wilkinson M. I., Wyse R. F. G., Kleyna J. T., Koch A., Evans N. W., Grebel E. K., 2007, ApJ, 663, 948
Gnedin O. Y., Kravtsov A. V., Klypin A. A., Nagai D., 2004, ApJ, 616, 16
Gnedin O. Y., Ceverino D., Gnedin N. Y., Klypin A. A., Kravtsov A. V., Levine R., Nagai D., Yepes G., 2011, preprint (arXiv:1108.5736)
Gómez-Vargas G. A. et al., 2013, J. Cosmol. Astropart. Phys., 10, 29
Governato F. et al., 2012, MNRAS, 422, 1231
Guedes J., Callegari S., Madau P., Mayer L., 2011, ApJ, 742, 76
Guo Q., White S., 2014, MNRAS, 437, 3228
Guo Q., White S., Li C., Boylan-Kolchin M., 2010, MNRAS, 404, 1111
Hinshaw G. et al., 2013, ApJS, 208, 19
Hopkins P. F., 2013, MNRAS, 428, 2840
Hopkins P. F., Kereš D., Oñorbe J., Faucher-Giguère C.-A., Quataert E., Murray N., Bullock J. S., 2014, MNRAS, 445, 581
Hu C.-Y., Naab T., Walch S., Moster B. P., Oser L., 2014, MNRAS, 443, 1173
Kennedy R., Frenk C., Cole S., Benson A., 2014, MNRAS, 442, 2487
Klypin A., Kravtsov A. V., Valenzuela O., Prada F., 1999, ApJ, 522, 82
Klypin A., Karachentsev I., Makarov D., Nasonova O., 2015, MNRAS, 454, 1798
Knollmann S. R., Knebe A., 2009, ApJS, 182, 608
Komatsu E. et al., 2011, ApJS, 192, 18
Kravtsov A., 2010, Adv. Astron., 2010, 8
Kravtsov A. V., Borgani S., 2012, ARA&A, 50, 353
Kravtsov A. V., Gnedin O. Y., Klypin A. A., 2004, ApJ, 609, 482
Macciò A. V., Stinson G., Brook C. B., Wadsley J., Couchman H. M. P., Shen S., Gibson B. K., Quinn T., 2012, ApJ, 744, L9
Madau P., Shen S., Governato F., 2014, ApJ, 789, L17
Mao S., Schneider P., 1998, MNRAS, 295, 587
Marinacci F., Pakmor R., Springel V., 2014a, MNRAS, 437, 1750
Marinacci F., Pakmor R., Springel V., Simpson C. M., 2014b, MNRAS, 442, 3745
Martinez G. D., 2015, MNRAS, 451, 2524
Mashchenko S., Couchman H. M. P., Wadsley J., 2006, Nature, 442, 539
Mashchenko S., Wadsley J., Couchman H. M. P., 2008, Science, 319, 174
Mayer L., Mastropietro C., Wadsley J., Stadel J., Moore B., 2006, MNRAS, 369, 1021
Mihos J. C., Hernquist L., 1996, ApJ, 464, 641
Mollitor P., Nezri E., Teyssier R., 2015, MNRAS, 447, 1353
Moore B., Ghigna S., Governato F., Lake G., Quinn T., Stadel J., Tozzi P., 1999, ApJ, 524, L19
Moster B. P., Naab T., White S. D. M., 2013, MNRAS, 428, 3121
Navarro J. F., Frenk C. S., White S. D. M., 1996, ApJ, 462, 563
Navarro J. F., Frenk C. S., White S. D. M., 1997, ApJ, 490, 493
Nelson D. et al., 2015, Astron. Comput., 13, 12
Ogiya G., Burkert A., 2015, MNRAS, 446, 2363
Okamoto T., 2013, MNRAS, 428, 718
Okamoto T., Frenk C. S., 2009, MNRAS, 399, L174
Okamoto T., Gao L., Theuns T., 2008, MNRAS, 390, 920
Okamoto T., Frenk C. S., Jenkins A., Theuns T., 2010, MNRAS, 406, 208
Onions J. et al., 2012, MNRAS, 423, 1200
Oñorbe J., Boylan-Kolchin M., Bullock J. S., Hopkins P. F., Keřes D., Faucher-Giguère C.-A., Quataert E., Murray N., 2015, MNRAS, 454, 2092
Papastergis E., Giovanelli R., Haynes M. P., Shankar F., 2015, A&A, 574, A113
Peñarrubia J., McConnachie A. W., Navarro J. F., 2008a, ApJ, 672, 904
Peñarrubia J., Navarro J. F., McConnachie A. W., 2008b, ApJ, 673, 226
Peñarrubia J., Benson A. J., Walker M. G., Gilmore G., McConnachie A. W., Mayer L., 2010, MNRAS, 406, 1290
Perlmutter S. et al., 1999, ApJ, 517, 565
Pillepich A., Kuhlen M., Guedes J., Madau P., 2014, ApJ, 784, 161
Planck Collaboration XIII 2015, preprint (arXiv:1502.01589)
Polisensky E., Ricotti M., 2014, MNRAS, 437, 2922
Pontzen A., Governato F., 2012, MNRAS, 421, 3464
Pontzen A., Governato F., 2014, Nature, 506, 171
Power C., Navarro J. F., Jenkins A., Frenk C. S., White S. D. M., Springel V., Stadel J., Quinn T., 2003, MNRAS, 338, 14
Puchwein E., Springel V., 2013, MNRAS, 428, 2966
Pujol A. et al., 2014, MNRAS, 438, 3205
Read J. I., Hayfield T., 2012, MNRAS, 422, 3037
Ricotti M., 2009, MNRAS, 392, L45
Riess A. G. et al., 1998, AJ, 116, 1009
Romano-Díaz E., Shlosman I., Heller C., Hoffman Y., 2010, ApJ, 716, 1095
Rubin V. C., Ford W. K. J., Thonnard N., 1980, ApJ, 238, 471
Ryden B. S., Gunn J. E., 1987, ApJ, 318, 15
Sawala T., Scannapieco C., White S., 2012, MNRAS, 420, 1714
Sawala T., Frenk C. S., Crain R. A., Jenkins A., Schaye J., Theuns T., Zavala J., 2013, MNRAS, 431, 1366
Sawala T. et al., 2014, preprint (arXiv:1412.2748)
Sawala T. et al., 2016, MNRAS, 456, 85
Scannapieco C. et al., 2012, MNRAS, 423, 1726
Schaller M. et al., 2015, MNRAS, 451, 1247
Schaye J. et al., 2015, MNRAS, 446, 521
Schneider A., Anderhalden D., Macciò A. V., Diemand J., 2014, MNRAS, 441, L6
Sijacki D., Springel V., Di Matteo T., Hernquist L., 2007, MNRAS, 380, 877
Sijacki D., Vogelsberger M., Kereš D., Springel V., Hernquist L., 2012, MNRAS, 424, 2999
Somerville R. S., Davé R., 2015, ARA&A, 53, 51
Spergel D. N. et al., 2007, ApJS, 170, 377
Springel V., 2010, MNRAS, 401, 791
Springel V., Hernquist L., 2003, MNRAS, 339, 289
Springel V., White S. D. M., Tormen G., Kauffmann G., 2001, MNRAS, 328, 726
Springel V., White S. D. M., Hernquist L., 2004, in Ryder S., Pisano D., Walker M., Freeman K., eds, Proc. IAU Symp. 220, Dark Matter in Galaxies. Astron. Soc. Pac., San Francisco, p. 421
Springel V., Di Matteo T., Hernquist L., 2005a, MNRAS, 361, 776
Springel V. et al., 2005b, Nature, 435, 629
Springel V., Frenk C. S., White S. D. M., 2006, Nature, 440, 1137
Springel V. et al., 2008, MNRAS, 391, 1685
Stinson G. S., Brook C., Macciò A. V., Wadsley J., Quinn T. R., Couchman H. M. P., 2013, MNRAS, 428, 129
Strigari L. E., Frenk C. S., White S. D. M., 2010, MNRAS, 408, 2364
Tegmark M. et al., 2006, Phys. Rev. D, 74, 123507
Teyssier R., Pontzen A., Dubois Y., Read J. I., 2013, MNRAS, 429, 3068
The Fermi-LAT Collaboration 2014, Phys. Rev. D, 89, 042001
Tollerud E. J., Boylan-Kolchin M., Bullock J. S., 2014, MNRAS, 440, 3511
Torrey P., Vogelsberger M., Sijacki D., Springel V., Hernquist L., 2012, MNRAS, 427, 2224
Velliscig M., van Daalen M. P., Schaye J., McCarthy I. G., Cacciato M., Le Brun A. M. C., Dalla Vecchia C., 2014, MNRAS, 442, 2641
Vera-Ciro C. A., Sales L. V., Helmi A., Frenk C. S., Navarro J. F., Springel V., Vogelsberger M., White S. D. M., 2011, MNRAS, 416, 1377
Vera-Ciro C. A., Helmi A., Starkenburg E., Breddels M. A., 2013, MNRAS, 428, 1696
Vikhlinin A., Kravtsov A., Forman W., Jones C., Markevitch M., Murray S. S., Van Speybroeck L., 2006, ApJ, 640, 691

Vogelsberger M., Zavala J., Loeb A., 2012, MNRAS, 423, 3740
Vogelsberger M., Genel S., Sijacki D., Torrey P., Springel V., Hernquist L., 2013, MNRAS, 436, 3031
Vogelsberger M. et al., 2014a, MNRAS, 444, 1518
Vogelsberger M., Zavala J., Simpson C., Jenkins A., 2014b, MNRAS, 444, 3684
Vogelsberger M. et al., 2014c, Nature, 509, 177
Wadepuhl M., Springel V., 2011, MNRAS, 410, 1975
Wang J., Frenk C. S., Navarro J. F., Gao L., Sawala T., 2012, MNRAS, 424, 2715
Weisz D. R., Dolphin A. E., Skillman E. D., Holtzman J., Gilbert K. M., Dalcanton J. J., Williams B. F., 2015, ApJ, 804, 136
Xu D. D., Mao S., Cooper A. P., Wang J., Gao L., Frenk C. S., Springel V., 2010, MNRAS, 408, 1721
Xu D., Sluse D., Gao L., Wang J., Frenk C., Mao S., Schneider P., Springel V., 2015, MNRAS, 447, 3189
Young P., 1980, ApJ, 242, 1232
Yurin D., Springel V., 2015, MNRAS, 452, 2343
Zemp M., Gnedin O. Y., Gnedin N. Y., Kravtsov A. V., 2011, ApJS, 197, 30
Zemp M., Gnedin O. Y., Gnedin N. Y., Kravtsov A. V., 2012, ApJ, 748, 54
Zhu Q., Hernquist L., Li Y., 2015, ApJ, 800, 6
Zolotov A. et al., 2012, ApJ, 761, 71
Zwicky F., 1937, ApJ, 86, 217

This paper has been typeset from a TEX/LATEX file prepared by the author.